MNRAS **445,** 4267–4286 (2014) doi:10.1093/mnras/stu1610

Are peculiar velocity surveys competitive as a cosmological probe?

Jun Koda,[1,2]★ Chris Blake,[1,2] Tamara Davis,[2,3,4] Christina Magoulas,[5] Christopher M. Springob,[2,6,7] Morag Scrimgeour,[2,6] Andrew Johnson,[1,2] Gregory B. Poole[5] and Lister Staveley-Smith[2,6]

[1]*Centre for Astrophysics and Supercomputing, Swinburne University of Technology, PO Box 218, Hawthorn, VIC 3122, Australia*
[2]*ARC Centre of Excellence for All-sky Astrophysics (CAASTRO)*
[3]*School of Mathematics and Physics, University of Queensland, Brisbane, QLD 4072, Australia*
[4]*Dark Cosmology Centre, Niels Bohr Institute, University of Copenhagen, Juliane Maries Vej 30, DK-2100 Copenhagen, Denmark*
[5]*School of Physics, University of Melbourne, Parkville, VIC 3010, Australia*
[6]*International Centre for Radio Astronomy Research, University of Western Australia, 35 Stirling Highway, Perth, WA 6009, Australia*
[7]*Australia Astronomical Observatory, PO Box 915, North Ryde, NSW 1670, Australia*

Accepted 2014 August 7. Received 2014 July 15; in original form 2013 December 3

ABSTRACT

Peculiar velocity surveys, which measure galaxy velocities directly from standard candles in addition to redshifts, can provide strong constraints on the growth rate of structure at low redshift. The improvement originates from the physical relationship between galaxy density and peculiar velocity, which substantially reduces cosmic variance. We use Fisher matrix forecasts to show that peculiar velocity data can improve the growth rate constraints by about a factor of 2 compared to density alone for surveys with galaxy number density of $10^{-2}\,(h^{-1}\,\mathrm{Mpc})^{-3}$, if we can use all the information for wavenumber $k \leq 0.2\,h\,\mathrm{Mpc}^{-1}$. In the absence of accurate theoretical models at $k = 0.2\,h\,\mathrm{Mpc}^{-1}$, the improvement over redshift-only surveys is even larger – around a factor of 5 for $k \leq 0.1\,h\,\mathrm{Mpc}^{-1}$. Future peculiar velocity surveys, Transforming Astronomical Imaging surveys through Polychromatic Analysis of Nebulae (TAIPAN), and the all-sky H I surveys, Widefield ASKAP L-band Legacy All-sky Blind Survey (WALLABY) and Westerbork Northern Sky H I Survey (WNSHS), can measure the growth rate to 3 per cent at $z \sim 0.025$. Although the velocity subsample is about an order of magnitude smaller than the redshift sample from the same survey, it improves the constraint by 40 per cent compared to the same survey without velocity measurements. Peculiar velocity surveys can also measure the growth rate as a function of wavenumber with 15–30 per cent uncertainties in bins with widths $\Delta k = 0.01\,h\,\mathrm{Mpc}^{-1}$ in the range $k \leq 0.1\,h\,\mathrm{Mpc}^{-1}$, which is a large improvement over galaxy density only. Such measurements on very large scales can detect signatures of modified gravity or non-Gaussianity through scale-dependent growth rate or galaxy bias. We test our modelling in detail using *N*-body simulations.

Key words: methods: numerical – cosmological parameters – cosmology: theory – large-scale structure of Universe.

1 INTRODUCTION

Whether the accelerated expansion of the Universe and the growth of the large-scale structure can be fully explained by the standard Λ cold dark matter (ΛCDM) model, especially by the cosmological constant Λ, is one of the main questions of modern cosmology. Dark energy, which can have an equation of state different from the cosmological constant, or theories of gravity alternative to general relativity, might be a source of recent accelerated expansion. Galaxy peculiar velocities provide powerful tests of the ΛCDM model through measurements of the linear growth rate, which are complementary to other cosmic probes. The linear growth rate, $f \equiv \mathrm{d}\ln D(a)/\mathrm{d}\ln a$, is the logarithmic derivative of the linear growth factor D with respect to the cosmic scale factor a. Different models of dark energy or modified gravity give different growth rates as a function of time or scale.

Observed redshift is a combined effect of cosmological expansion which depends on the distance to the source, and the Doppler shift which depends on the peculiar velocity of the light source.

★ E-mail: junkoda@physics.utexas.edu

Direct measurements of line-of-sight peculiar velocities from redshifts and distances determined by the Tully–Fisher relation, Fundamental Plane, or supernovae have a long history (see Strauss & Willick 1995, for a review). Latest peculiar velocity surveys have increased their samples to about 5000 Tully–Fisher velocities (Springob et al. 2007), and 9000 Fundamental Plane velocities (Magoulas et al. 2012). Supernovae samples are also competitive because the smaller sample size is compensated by their better precision per measurement (Turnbull et al. 2012; Feindt et al. 2013). Future surveys plan to expand peculiar velocity samples further, as we present in this paper. All of these samples are limited to low redshift ($z \lesssim 0.05$), because the velocity error grows at least linearly with distance, 8–25 per cent of the Hubble recession velocity, due to intrinsic scatter in distance estimation.

A completely different path to measure peculiar velocity is the kinetic Sunyaev–Zel'dovich effect (Sunyaev & Zeldovich 1980), which measures line-of-sight velocities of galaxies or clusters of galaxies with respect to the cosmic microwave background (CMB). The bulk motion of electrons along the large-scale peculiar velocity field make a tiny contribution to the CMB temperature via Thomson scattering between CMB photons and free electrons in galaxies or clusters. The kinetic Sunyaev–Zel'dovich effect has just started to be measurable (Hand et al. 2012; Lavaux, Afshordi & Hudson 2013), and has the potential to provide peculiar velocity measurements with errors that do not diverge linearly with distance.

Alternatively, the information of line-of-sight peculiar velocity is also encoded in the anisotropic pattern of large-scale galaxy clustering, known as the redshift-space distortion (Kaiser 1987). Many measurements of growth rates through redshift-space distortion have been made across wide ranges of redshifts (e.g. Peacock et al. 2001; Tegmark et al. 2004; Guzzo et al. 2008; Blake et al. 2011; Beutler et al. 2012; de la Torre et al. 2013; Samushia et al. 2013). These measurements are, so far, all consistent with the ΛCDM Universe, and continue to improve in precision and redshift range (e.g. White, Song & Percival 2009; Amendola et al. 2013a; de Putter, Doré & Takada 2013; Weinberg et al. 2013). In this paper, we refer to these measurements as those from 'galaxy density only', 'redshift-space distortions only', or 'redshift only', interchangeably, to distinguish them from peculiar velocity surveys.

CMB measurements constrain cosmological parameters precisely within the ΛCDM cosmological model, but are not as sensitive to low-redshift growth of structure. Peculiar velocity surveys therefore allow a powerful consistency check of scenarios of dark energy or modified theories of gravity. Low-redshift data are useful as these correspond to the epoch when the ratio of dark energy density to critical density is the largest and where any deviation from ΛCDM is likely to be the most significant (Hudson & Turnbull 2012).

The amplitude of velocity fluctuation measures $f\sigma_8$ where σ_8 is the amplitude of matter perturbation smoothed on spheres of $8\,h^{-1}\,\mathrm{Mpc}$, and h is the Hubble constant in units of $100\,\mathrm{km\,s^{-1}\,Mpc^{-1}}$. The velocity power spectrum (Jaffe & Kaiser 1995; Abate & Erdoğdu 2009; Macaulay et al. 2011) measures $f\sigma_8$ as a function of wavenumber, and the bulk flow (Kaiser 1988; Watkins, Feldman & Hudson 2009) or low-order moments (Feldman, Watkins & Hudson 2010) of the velocity field are a cross-check of the model at large scales. Many bulk flow measurements show that the local velocity fluctuations at large scales are larger than found at a typical location in the ΛCDM Universe, but whether the large bulk flow is inconsistent with the ΛCDM Universe (Watkins et al. 2009; Feldman et al. 2010) or consistent (Nusser & Davis 2011; Turnbull et al. 2012; Ma & Scott 2013) is still under debate. Since we can only measure the large-scale bulk flow around us, it is not decisive (from velocity data alone) whether the large-scale velocities are a problem of the ΛCDM universe or a statistical outcome that we are simply in a high-velocity region of the ΛCDM Universe (cosmic variance).

One of the advantages of peculiar velocity surveys is that they have multiple tracers, galaxy density, and peculiar velocity, which can be used to measure growth rate beyond the cosmic variance limit. In contrast, methods that use only one tracer of large-scale structure are limited by the number of fluctuation modes in the observed volume. In the case of peculiar velocity surveys, cosmic variance can be reduced by first predicting the expected velocity field from the galaxy distribution (Nusser & Davis 1994; Branchini, Eldar & Nusser 2002; Erdoğdu et al. 2006; Kitaura & Enßlin 2008; Lavaux et al. 2010; Kitaura et al. 2012), and then comparing the model velocities with the observed velocities. The ratio of the two gives the $\beta \equiv f/b$ parameter, where b is the galaxy bias (Davis, Nusser & Willick 1996; Branchini et al. 2001; Davis et al. 2011; Ma, Branchini & Scott 2012). Throughout this study we assume linear bias between galaxies and matter, although we note that for models with significant non-Gaussianity, or at small scales, this relation would break down. However, the signal-to-noise ratio of peculiar velocity measurements peaks on large scales, where linear bias is a common approximation. Because the reconstructed velocity and the observed velocity share the same random perturbation, the measurement of β is not limited by the cosmic variance, but continues to improve as the statistical error of velocities is reduced by increasing the number of velocity measurements. To obtain a more fundamental quantity, which does not depend on galaxy selection through bias b, one can obtain $f\sigma_8$ by multiplying β by the amplitude of the galaxy clustering, $b\sigma_8$. Similar techniques for going beyond the cosmic variance limit have also been proposed by using multiple populations of galaxy densities with different biases instead of density and velocity (McDonald & Seljak 2009; Gil-Marín et al. 2010; Bernstein & Cai 2011).

The dependence of the growth rate on the wavenumber k is also an important observable for distinguishing theories of gravity (e.g. Song & Percival 2009; Jennings et al. 2012; Amendola et al. 2013b; Asaba et al. 2013; Taruya et al. 2014). Although the overall normalization of β depends on galaxy bias b, we can test whether β is independent of k, as predicted by general relativity. Similarly, scale dependence of β can also constrain primordial non-Gaussianity which generates scale-dependent bias (Dalal et al. 2008; Matarrese & Verde 2008; Slosar et al. 2008; Desjacques, Seljak & Iliev 2009; Adshead et al. 2012; D'Aloisio et al. 2013). The advantage of multiple tracers over a single tracer become larger for testing the scale dependence than for the case of assuming constant β, improving the constraints especially at low k by evading the cosmic variance (Seljak 2009; Hamaus, Seljak & Desjacques 2011; Ma, Taylor & Scott 2013).

The purpose of this paper is to investigate whether future peculiar velocity surveys are competitive with redshift surveys, and evaluate how much the peculiar velocity data improve the constraints on the growth rates $f\sigma_8$ and β. Burkey & Taylor (2004) introduced the Fisher matrix analysis to peculiar velocity surveys, and forecast the performance of the 6dF Galaxy Survey peculiar velocity survey (6dFGSv; Jones et al. 2009; Magoulas et al. 2012). Since their paper simply uses the linear velocity power spectrum without redshift-space distortions, we first improve the model equations for auto- and cross-power spectra of galaxy density and peculiar velocity by comparing the equations with an N-body simulation in Section 2. Using the model, we show how constraints from peculiar velocity

surveys improve compared with those from redshift surveys, using the Fisher matrix formalism in a general case in Section 3. We present our new forecast for future peculiar velocity surveys in Section 4, and summarize the results in Section 5. Throughout the paper, we use a flat ΛCDM cosmology with $\Omega_{\rm m} = 0.273$, $\Omega_\Lambda = 0.727$, $\Omega_{\rm b} = 0.0546$, $h = 0.705$, $\sigma_8 = 0.812$, and $n_{\rm s} = 0.961$.

2 VELOCITY POWER SPECTRUM IN REDSHIFT SPACE

In this section, we introduce simple model equations that describe the auto- and cross-power spectra of galaxy number density and line-of-sight velocity *in redshift space*. Although real-space distances to galaxies are in principle measurable in peculiar velocity surveys, we assume that analyses are performed in redshift space. This is because the velocity measurement errors are sufficiently large that the real-space location has a significant error, complicating clustering measurements, whereas the redshift-space position is accurately known. We use these model equations to calculate the Fisher matrix in Section 3, assuming the density and velocities are Gaussian random fields completely characterized by the power spectra.

We denote the galaxy density contrast field by $\delta_{\rm g}$, the velocity vector field by $\boldsymbol{v}$, and the line-of-sight velocity by u, respectively. We focus on the line-of-sight velocity, instead of the velocity vector or the velocity divergence, because the line-of-sight velocity is the observable in peculiar velocity surveys. Throughout the paper, we assume the flat-sky approximation, such that the line of sight is fixed to the third axis: $u \equiv v_3$. Analysis of real data samples would incorporate curved-sky effects, but the flat-sky approximation is necessary for the forecasting approach outlined here and does not affect the relative comparison of surveys.

The auto- and cross-power spectra of δ and u are ensemble averages of their products in Fourier space: $P_{\rm gg}(\boldsymbol{k}) = V^{-1}\langle\delta_{\rm g}(\boldsymbol{k})\delta_{\rm g}(\boldsymbol{k})^*\rangle$, $P_{\rm gu}(\boldsymbol{k}) = V^{-1}\langle\delta_{\rm g}(\boldsymbol{k})u(\boldsymbol{k})^*\rangle$, and $P_{\rm uu}(\boldsymbol{k}) = V^{-1}\langle u(\boldsymbol{k})u(\boldsymbol{k})^*\rangle$, where V is a volume of a periodic box, and $\delta_{\rm g}(\boldsymbol{k})$ and $u(\boldsymbol{k})$ are the Fourier transform of $\delta_{\rm g}(\boldsymbol{x})$ and $u(\boldsymbol{x})$, respectively, for a convention that the Fourier transformation of a function $f(\boldsymbol{x})$ is $f(\boldsymbol{k}) = \int_V f(\boldsymbol{x})\mathrm{e}^{-\mathrm{i}\boldsymbol{k}\cdot\boldsymbol{x}}\mathrm{d}^3x$.

Although the cross-power spectrum is generally a complex-valued function, the cross-power of $\delta_{\rm g}$ and u has a purely imaginary value by parity invariance. If you flip the Universe to the mirror image, $\boldsymbol{x} \mapsto -\boldsymbol{x}$ and $u \mapsto -u$, the ensemble averaged quantities, including the cross power, must be the same, because the statistical property of the initial condition and the time evolution by gravity are both indistinguishable under this parity transformation. Fourier modes transform as $\delta_{\rm g}(\boldsymbol{k}) \mapsto \delta_{\rm g}(-\boldsymbol{k})$ and $u(\boldsymbol{k}) \mapsto -u(-\boldsymbol{k})$, respectively, under the parity transformation. This argument leads to, $V P_{\rm gu}(\boldsymbol{k}) = \langle\delta_{\rm g}(\boldsymbol{k})u(\boldsymbol{k})^*\rangle = -\langle\delta_{\rm g}(-\boldsymbol{k})u(-\boldsymbol{k})^*\rangle = -\langle\delta_{\rm g}^*(\boldsymbol{k})u(\boldsymbol{k})\rangle = -V P_{\rm gu}(\boldsymbol{k})^*$, where the reality condition $f(-\boldsymbol{k}) = f(\boldsymbol{k})^*$, for any real function $f(\boldsymbol{x})$, is used. This shows that $P_{\rm gu}$ is pure imaginary. Note that this is true for the ensemble average with infinite volume or infinite number of random realizations; $P_{\rm gu}$ estimated from a finite number of modes is consistent with pure imaginary only within statistical uncertainty. This property of having either a real or a pure imaginary off-diagonal element is not limited to linear perturbation theory, but also applicable to non-linear power spectra.

Since the vorticity $\nabla \times \boldsymbol{v}$ is negligible on large scales (Pueblas & Scoccimarro 2009), the line-of-sight velocity field is directly related to the velocity divergence field, $\theta(\boldsymbol{x}) \equiv -\nabla \cdot \boldsymbol{v}(\boldsymbol{x})/(aHf)$, to a good approximation on the scales we are interested in, where $H = H(z)$ is the Hubble parameter at redshift z. The corresponding relation in Fourier space is

$$u(\boldsymbol{k}) = -\mathrm{i}aHf\mu\theta(\boldsymbol{k})/k, \quad (1)$$

where $k \equiv |\mathbf{k}|$, and μ is the cosine of the angle between $\boldsymbol{k}$ and the line of sight, $\mu \equiv k_3/k$. The continuity equation relates the velocity divergence field to the time derivative of the density field. The θ variable is defined such that it is equal to δ in the linear limit: $\theta(\boldsymbol{k}) = \delta_{\rm m}(\boldsymbol{k})$. We review the N-body simulation in Section 2.1, and present the power spectra in real space in Section 2.2. In Section 2.3, we introduce the model equations in redshift space, and test those equations using the simulation.

2.1 The simulation

We use subhaloes in the GiggleZ simulation (Poole et al., in preparation) to calculate simulated galaxy and velocity power spectra. The simulation has 2160^3 N-body particles of masses $7.5 \times 10^9\, h^{-1}\,\mathrm{M}_\odot$, in a periodic box of $1\, h^{-1}$ Gpc on a side. The cosmological parameters used in this simulation are listed at the end of Section 1. Although each forecast depends in detail on the fiducial cosmological model, the relative performance of peculiar velocity and redshift-space distortion surveys is much less sensitive to this and we expect our conclusions to be robust. The simulation is performed with the GADGET2 code (Springel 2005), and haloes and subhaloes are found by the SUBFIND code (Springel et al. 2001). We mainly present the results for subhaloes in the mass range $10^{11.5}$–$10^{12}\, h^{-1}\,\mathrm{M}_\odot$, which roughly correspond to disc galaxies observed in H I surveys, but our results are qualitatively the same for other subhaloes.

We compute the subhalo density field on a grid with the cloud-in-cell (CIC) method. The computation of the velocity field has technical difficulties that do not exist for the density field; for example, using the CIC method for the velocity would cause a problem of undefined velocities when the density of the cell is zero (see e.g. Pueblas & Scoccimarro 2009; Jennings 2012). We assign the line-of-sight velocity field on a 512^3 grid using the nearest particle method, i.e. for each grid point, we assign the velocity of the nearest particle to the grid. We fast Fourier transform the grids and calculate their auto- and cross-power spectra. We subtract shot noise from the galaxy auto-power spectrum, and correct for the smoothing and aliasing caused by gridding. We explain the details of this process in Appendix A, which enables us to construct reliable power spectra and hence the model equations. Numerical errors caused by gridding are less than 1 per cent for $k \leq 0.2\, h\,\mathrm{Mpc}^{-1}$ after the corrections; our density and velocity power spectra are sufficiently accurate for our purpose. Our code for calculating the velocity power spectrum with the nearest particle method is publicly available at https://github.com/junkoda/np_vpower.

2.2 The power spectra in real space

In this section, we present the angle-averaged auto- and cross-power spectra in real space; we discuss the power spectra in redshift space in Section 2.3. We angle average the power spectra in the upper-half of Fourier space, which corresponds to an integral $\int_0^1 \mathrm{d}\mu$ in the continuous limit, $V \to \infty$. We average the products of Fourier modes in equally spaced bins with width $\Delta k = 0.01\, h\,\mathrm{Mpc}^{-1}$, and plot the result against the averages of the magnitudes k in the bins in Fig. 1. The redshift is $z = 0$, and the mass range of the subhaloes

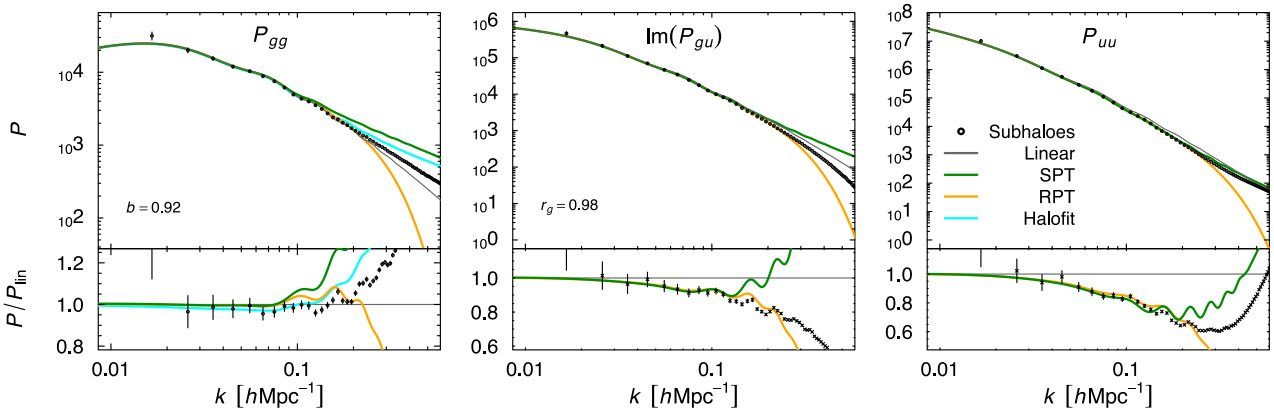

Figure 1. The angle-averaged auto- and cross-power spectra for galaxy density and line-of-sight peculiar velocity in real space. The three panels for $P_{\rm gg}$, $P_{\rm gu}$, and $P_{\rm uu}$ are for the galaxy auto-power spectrum, galaxy–velocity cross-power spectrum, and velocity auto-power spectrum, respectively. The points are from subhaloes in the GiggleZ simulation, grey lines are linear theory, green lines are one-loop SPT, and orange lines are one-loop RPT. The blue line for $P_{\rm gg}$ is the prediction of HALOFIT. The overall amplitudes of the theoretical curves are scaled by linear bias b and galaxy-matter cross-correlation coefficient, $r_{\rm g}$ (equations 3–5). The units of the power spectra $P_{\rm gg}$, $P_{\rm gu}$, and P are $(h^{-1}\,\mathrm{Mpc})^3$, $100\,\mathrm{km\,s^{-1}}\,(h^{-1}\,\mathrm{Mpc})^3$, and $(100\,\mathrm{km\,s^{-1}})^2\,(h^{-1}\,\mathrm{Mpc})^3$, respectively. In the bottom panels, we plot the power spectra divided by the linear power spectra. The real-space power spectra are described by existing theoretical curves reasonably well.

is $(10^{11.5}$–$10^{12})\,h^{-1}\,\mathrm{M}_\odot$. Error bars indicate the uncertainty due to cosmic variance and shot noise:

$$\Delta P_{\rm gg} = (P_{\rm gg} + \bar{n}^{-1})/\sqrt{N_k}, \tag{2}$$

where N_k is the number of modes in the bin, and $\bar{n} = 5.4 \times 10^{-3}\,(h^{-1}\,\mathrm{Mpc})^{-3}$ is the subhalo number density. We do not add the shot noise to the error bars for the cross-power and the velocity autopower spectrum: $\Delta P = P/\sqrt{N_k}$.

We plot the power spectra calculated from perturbation theories as the lines in Fig. 1 – the linear perturbation theory, the one-loop standard perturbation theory (SPT; see Bernardeau et al. 2002, for a review), and the one-loop renormalized perturbation theory (RPT; Crocce & Scoccimarro 2006). We also plot the HALOFIT power spectrum (Smith et al. 2003; Takahashi et al. 2012) for the galaxy–galaxy autopower. We use publicly available codes CAMB[1] (Lewis, Challinor & Lasenby 2000) for the linear and the HALOFIT matter power spectra. We calculate the matter-velocity divergence auto- and cross-power spectra, $P_{\rm mm}$, $P_{{\rm m}\theta}$, and $P_{\theta\theta}$, using the Cosmology Routine Library[2] (Jeong & Komatsu 2006) for the SPT, and the COPTER package by Carlson, White & Padmanabhan (2009) for the one-loop RPT.[3] All three power spectra are equal to each other in the linear order: $P_{\rm mm} = P_{{\rm m}\theta} = P_{\theta\theta}$. We fit the N-body result with two free parameters, the linear galaxy bias b and the galaxy–matter cross-correlation coefficient $r_{\rm g}$:

$$P_{\rm gg}(k) = b^2 P_{\rm mm}(k), \tag{3}$$

$$P_{\rm gu}(k) = \mathrm{i}aHf\mu b r_{\rm g} P_{{\rm m}\theta}(k)/k, \tag{4}$$

$$P_{\rm uu}(k) = (aHf\mu/k)^2 P_{\theta\theta}(k). \tag{5}$$

These functional forms follow from the relation between u and θ in equation (1). The galaxy correlation coefficient can be less than 1 if there is a stochastic bias (Dekel & Lahav 1999). We calculate the best-fitting bias value $b = 0.92$ by minimizing the χ^2 between the simulation and the HALOFIT power spectra, and find the best-fitting correlation coefficient value $r_{\rm g} = 0.98$ by similarly fitting between simulation and RPT cross-power $P_{\rm gu}$ for the fixed best-fitting b, both in the range $k \leq 0.1\,h\,\mathrm{Mpc}^{-1}$. We assign equation (2) for the statistical uncertainty in the power spectra. The figure shows that the one-loop perturbation theories are in reasonable agreement with the simulation result.

[1] http://camb.info
[2] http://www.mpa-garching.mpg.de/komatsu/crl/
[3] http://mwhite.berkeley.edu/Copter/

2.3 The power spectra in redshift space

2.3.1 The model in redshift space

We follow the prescription of modelling density and velocity power spectra by Burkey & Taylor (2004, hereafter BT04), and improve their model by introducing a new damping term $D_{\rm u}$ for the redshift-space distortion of the velocity field. Although BT04 use the velocity derivative instead of velocity, both quantities give the same Fisher matrix forecast, as we see later. The galaxy clustering is modelled by a linear galaxy bias $b = \sqrt{P_{\rm gg}/P_{\rm mm}}$ and a galaxy–mass cross-correlation coefficient $r_{\rm g} = P_{\rm gm}/\sqrt{P_{\rm gg}P_{\rm mm}}$. The redshift-space distortion introduces additional perturbation in mass distribution, described by the Jacobian of the real-to-redshift-space mapping, known as the Kaiser squashing effect (Kaiser 1987). Unlike the density or the momentum, the velocity does not have the squashing term. The same Jacobian term for the density and momentum cancels each other for the velocity, which is the momentum divided by the density. We model the redshift-space distortion by the Kaiser factor and a damping term (Peacock & Dodds 1994) with the Lorentzian function (Ballinger, Peacock, & Heavens 1996):

$$D_{\rm g}(k,\mu)^2 \equiv [1 + (k\mu\sigma_{\rm g})^2/2]^{-1}, \tag{6}$$

where $\sigma_{\rm g}$ is a constant related to the pairwise velocity dispersion. Previous literature does not include the redshift-space distortions in the velocity field (i.e. sets $D_{\rm u} = 1$).

Our model equations for the auto- and cross-power spectra of galaxy and line-of-sight velocity in redshift space, $P^{\rm s}_{\rm gg}$, $P^{\rm s}_{\rm gu}$, and

Table 1. The best-fitting model parameters for subhaloes in various mass ranges, $\log_{10}[M/(1\,h^{-1}\,\mathrm{M}_\odot)] = 11.5$–12.0, 12.0–12.5, 12.5–13.0, and 13.0–13.5, in addition to the subhalo number density $\bar{n}$ in $(h^{-1}\,\mathrm{Mpc})^{-3}$. The damping parameters σ_g and σ_u are in $h^{-1}\,\mathrm{Mpc}$, and the random velocity parameter σ_* is in $\mathrm{km\,s^{-1}}$, respectively. All of these parameters depend on the subhalo population.

Mass range	$\bar{n}$	b	r_g	σ_g	σ_u	σ_*
11.5–12.0	5.4×10^{-3}	0.92	0.98	5.8	13.0	197
12.0–12.5	2.0×10^{-3}	1.0	0.96	5.1	13.9	186
12.5–13.0	6.8×10^{-4}	1.2	0.94	4.3	14.4	185
13.0–13.5	2.1×10^{-4}	1.5	0.92	3.1	15.4	195

P^s_uu, are the following:

$$P^\mathrm{s}_\mathrm{gg}(k,\mu) = (1 + 2r_\mathrm{g}\beta\mu^2 + \beta^2\mu^4)D_\mathrm{g}^2 b^2 P_\mathrm{mm}(k), \quad (7)$$

$$P^\mathrm{s}_\mathrm{gu}(k,\mu) = \mathrm{i}aHf\mu(r_\mathrm{g} + \beta\mu^2)D_\mathrm{g}D_\mathrm{u}bP_{\mathrm{m}\theta}(k)/k, \quad (8)$$

$$P^\mathrm{s}_\mathrm{uu}(k,\mu) = (aHf\mu/k)^2 D_\mathrm{u}^2 P_{\theta\theta}(k), \quad (9)$$

where $\beta \equiv f/b$. We expect that these equations hold only on large scales, $k \lesssim 0.2\,h\,\mathrm{Mpc}^{-1}$; non-linearity and scale-dependent bias become important for higher k. As we show below, we found strong damping in the cross- and velocity autopower spectra. We empirically fit the simulation results by a sinc function:

$$D_\mathrm{u}(k) \equiv \sin(k\sigma_\mathrm{u})/(k\sigma_\mathrm{u}), \quad (10)$$

where the constant σ_u is about $13\,h^{-1}\,\mathrm{Mpc}$ at $z = 0$ with a small dependence on halo mass (see Table 1). The model of equation (10) applies to scales $k \leq 0.2\,h\,\mathrm{Mpc}^{-1}$. In the following, we compare this model with the simulation in redshift space.

2.3.2 *Fitting the model parameters*

We compute the redshift-space distortion in the simulation by shifting the line-of-sight coordinates of subhaloes: $x_3 \mapsto x_3 + u/(aH)$, and measure the power spectra in the same way as in real space. In Fig. 2, we show that our model equations for the redshift space are in good agreement with the simulation. In the upper panels, we show the angle-averaged auto- and cross-power spectra in redshift space; points are calculated from subhaloes in the *N*-body simulation, dashed lines are the model equations in real space (equations 3–5), and the red solid lines are our model equations in redshift space (equations 7–9). The shot noise is subtracted from the galaxy autopower spectrum. We use the HALOFIT model for P_mm, and RPT for $P_{\mathrm{m}\theta}$ and $P_{\theta\theta}$, respectively. We find the best-fitting damping constant $\sigma_\mathrm{g} = 5.8\,h^{-1}\,\mathrm{Mpc}$ by fitting the model equation for the angle-averaged P^s_gg to the simulation data with minimum χ^2 for $k \leq 0.2\,h\,\mathrm{Mpc}^{-1}$, with fixed values of b and r_g which we have obtained by fitting the real-space power spectra. Similarly, we find the best-fitting damping constant for the velocity, $\sigma_\mathrm{u} = 13.0\,h^{-1}\,\mathrm{Mpc}$, by fitting the angle-averaged cross-power P^s_gu for fixed b, r_g, and σ_g. The angle-average integrals of the model equations (7)–(9) can be performed analytically with elementary functions.

2.3.3 *The cross-power spectrum*

The cross-power spectrum in redshift space becomes negative at $k = 0.23\,h\,\mathrm{Mpc}^{-1}$, and returns to positive values at $k = 1.06\,h\,\mathrm{Mpc}^{-1}$. This damping in velocity is much larger than that affecting the galaxy autopower spectrum; it is a 50 per cent effect at $k = 0.1\,h\,\mathrm{Mpc}^{-1}$, and damps to almost zero at $k = 0.2\,h\,\mathrm{Mpc}^{-1}$. The large damping cannot be explained by uncorrelated random velocities, in contrast to the damping in the density field (Peacock & Dodds 1994), because such random displacement would give the same damping for all three auto- and cross-spectra. The complete correlation between the velocity field and redshift-space displacement might be the origin of this large damping. We leave explanations of this strong damping to future studies. Our empirical damping formula is a good fit for $k \leq 0.2\,h\,\mathrm{Mpc}^{-1}$, which is sufficient for our Fisher matrix forecast, but does not capture the shape of negative cross-power spectrum for $k > 0.23\,h\,\mathrm{Mpc}^{-1}$. Because of this oscillating feature, a positive damping function, such as a Gaussian or Lorentzian, cannot fit the velocity cross-power spectrum well.

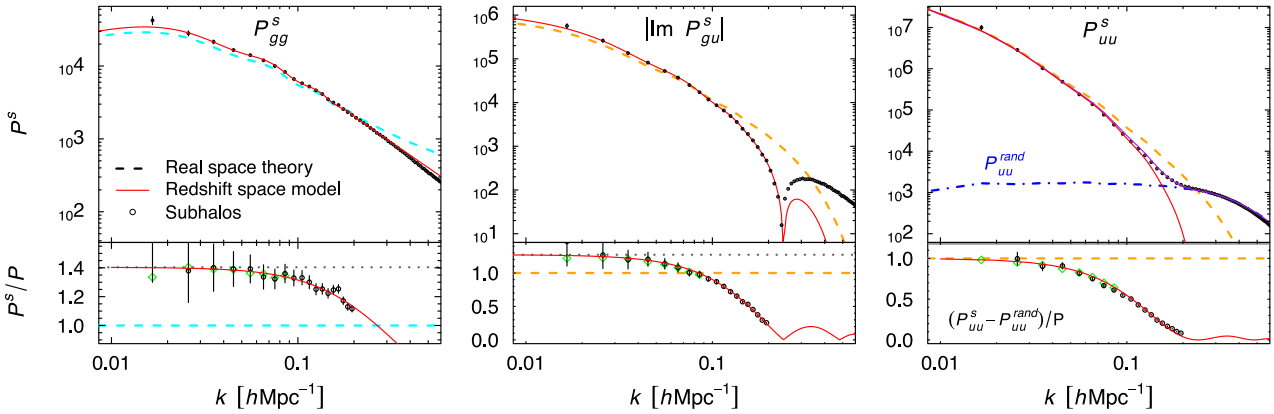

Figure 2. The angle-averaged auto- and cross-power spectra of density and peculiar velocity in redshift space. The superscript s denotes that the power spectra are in redshift space. Our model equations (solid red lines) are in good agreement with the subhaloes in the GiggleZ simulation (points). The dashed lines are theoretical power spectra in real space. Bottom panels show the ratio of power spectra in redshift space to those in real space. The dotted lines are the Kaiser limit. The deviations from the horizontal lines show the redshift-space damping. The circles are the simulation data divided by the theoretical real-space curve, while the green diamond points at low k are those divided by the simulation power spectra in real space. In the top right-hand panel, the random velocity component is shown by the blue dash–dotted line, and the model including the random term $P^\mathrm{rand}_\mathrm{uu}$ is plotted by the purple solid curve. In the bottom right-hand model, the random term is subtracted from the velocity power spectrum. We find strong damping in the density–velocity cross-power and velocity autopower spectra.

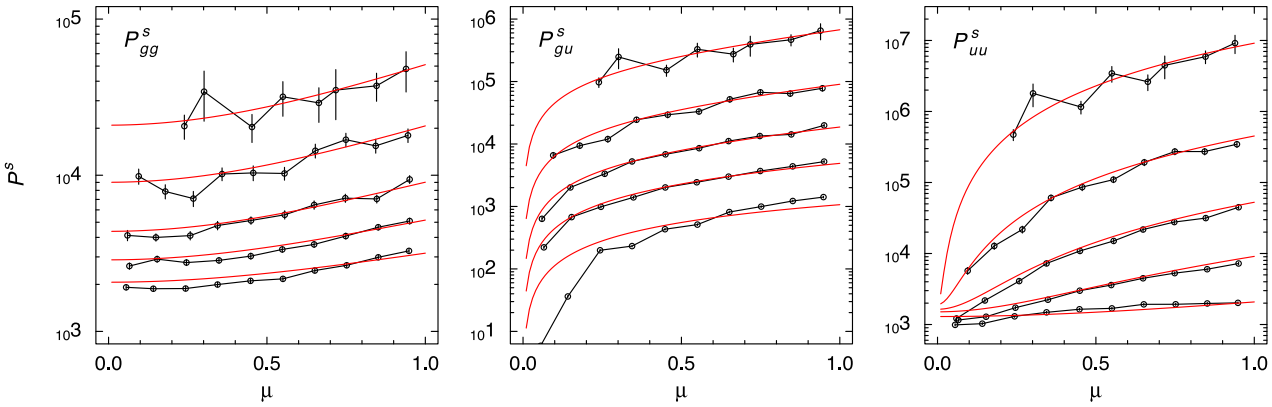

Figure 3. The dependence of power spectra on the angle μ to the line of sight in redshift space. The points are calculated from subhaloes averaged in bins with widths $\Delta\mu = 0.1$ and $\Delta k = 0.01$, at $k = 0.025, 0.065, 0.105, 0.405$, and $0.185\,h\,\mathrm{Mpc}^{-1}$. The red lines are the models with Kaiser effect and damping (equations 7–9). See Fig. 1 for the units of the power spectra.

2.3.4 *The velocity autopower spectrum*

We can explain the velocity autopower spectrum in redshift space with the same damping function D_u, and an additional *random velocity component* $P^\mathrm{rand}_\mathrm{uu}$, which is plotted with a blue dash–dotted line in the top right-hand panel of Fig. 2. We compute $P^\mathrm{rand}_\mathrm{uu}$ by assigning independent Gaussian random velocities with zero mean and standard deviation σ_* to subhaloes in redshift space. We find the best-fitting value $\sigma_* = 197\,\mathrm{km\,s}^{-1}$ by fitting the angle-averaged P^s_uu by the sum of equation (9) and $P^\mathrm{rand}_\mathrm{uu}$, for fixed σ_u. We fit for $k \leq 0.4\,h\,\mathrm{Mpc}^{-1}$ because we can determine the value of σ_* well at high k where the random component is dominant. We plot the sum of two terms by the solid purple line, which shows a good fit to the subhalo data. The random velocity component $P^\mathrm{rand}_\mathrm{uu}$ is analogous to the shot noise in galaxy autopower spectrum, in the sense that they are both inversely proportional to the galaxy number density, but $P^\mathrm{rand}_\mathrm{uu}$ also depends on the virial velocities of the galaxies. We find that the value of σ_* for haloes is smaller than that for the subhaloes, which is consistent with our interpretation that σ_* is related to virial motions.

In the bottom panels of Fig. 2, we plot the ratios of power spectra in redshift space to those in real space. The black circles are N-body data divided by the model equations in real space, while the green diamond points for $k \leq 0.1\,h\,\mathrm{Mpc}^{-1}$ are the same N-body data but divided by the real-space power spectra calculated from the N-body simulation. The grey dotted lines show the Kaiser limits, which do not have the damping factors. The data points from the simulation are in good agreement with our model equations with damping, plotted by the red lines.

2.3.5 *The angular dependence*

In Fig. 3, we plot the auto- and cross-power spectra as a function of wave vector angle μ for fixed k. Although $k\mu$ is the natural combination for redshift-space distortion, we do not see a clear dependence of the velocity damping on μ. We therefore choose a damping factor that only depends on $k = |\boldsymbol{k}|$, which is a reasonably good fit for the overall behaviour.

Figs 2 and 3 show that the simple models are consistent with the N-body simulation. The best-fitting model parameters depend on the subhalo sample. We summarize the parameters in Table 1. For more precise comparisons between simulations and recent models of galaxy or halo power spectrum in redshift space, see, for example, Nishimichi & Taruya (2011), Kwan, Lewis & Linder (2012), de la Torre & Guzzo (2012), Okumura, Seljak & Desjacques (2012), Ishikawa et al. (2014). Although we do not need accurate models for the Fisher matrix forecast, such accurate models are important to extract unbiased parameters from data, and increase the information by extending the range of k that can fit data without systematic error. Similar work is necessary for the velocity power spectrum to analyse future peculiar velocity data with high accuracy. For example, we do not include velocity bias in our model (Desjacques & Sheth 2010; Elia, Ludlow & Porciani 2012).

3 THE FISHER MATRIX FOR GALAXY NUMBER DENSITY AND VELOCITY

The Fisher information matrix $\mathbf{F}$ provides the best possible confidence intervals of unknown parameters, θ_i, such as $f\sigma_8, \beta$, or Ω_m, under the assumption that the likelihood function can be approximated by a multivariate Gaussian about the maximum likelihood. The inverse matrix $\mathbf{F}^{-1}$ gives the covariance matrix of the parameters θ_i, and $\Delta\theta_i = (F^{-1})_{ii}$ gives the 1σ uncertainty in θ_i, marginalized over all the other parameters. In the context of large-scale structure, the Fisher matrix forecasts the uncertainties in cosmological parameters that can be determined from given observational uncertainties in the power spectrum, which consist of sample variance of random density fluctuations, and shot noise from finite number of galaxies (Tegmark 1997; Tegmark et al. 1998). Observational error in peculiar velocity propagates to uncertainties for the velocity power spectrum (BT04).

We first review the Fisher matrix for the galaxy number density δ_g and the line-of-sight velocity u in Section 3.1. As BT04 do not show the detailed derivation of the Fisher matrix with spatially varying noise term, and the nice derivation by Abramo (2012) only focuses on the uncertainty of power spectra (not of parameters θ_i in general), we summarize the mathematical derivation of the Fisher matrix in Appendix B1, following Abramo (2012). The Fisher matrix for N multiple tracers (which can be a combination of density and velocity, or multiple density fields with different galaxy bias) has two formulae that are apparently different; one is written as a trace of $N \times N$ covariance matrices of Gaussian density fields (McDonald & Seljak 2009), and the other is written as a bilinear form with the $N(N+1)/2$-dimensional covariance matrix of power spectra (BT04; White et al. 2009). We show in the appendix that these two formulae

are algebraically equal to each other. As a result, the Fisher matrix we use in this paper is exactly equal to that used by BT04.

We note that a Fisher matrix study only provides a statistical comparison of forecast errors, ignoring systematics. Peculiar velocity surveys contain potential sources of systematic error not considered in our analysis, including calibration of the standard candle distances and non-Gaussianity in the resulting distance errors, selection-function effects from the distribution of objects on the sky, and non-linear effects in the modelling of velocities in redshift space. Whilst it is beyond the scope of this study to exhaustively quantify systematic effects, we note that efforts are continuing to address these effects in data and simulations, for example as presented by Davis et al. (2011), Magoulas et al. (2012), and Johnson et al. (2014).

3.1 The basic equations

The Fisher matrix for a multivariate Gaussian random variable with mean vector $\boldsymbol{\mu}$ and covariance matrix $\mathbf{C}$ is

$$F_{ij} = \frac{\partial \boldsymbol{\mu}^{\mathrm{T}}}{\partial \theta_i} \mathbf{C}^{-1} \frac{\partial \boldsymbol{\mu}}{\partial \theta_j} + \frac{1}{2} \mathrm{tr} \left[\mathbf{C}^{-1} \frac{\partial \mathbf{C}}{\partial \theta_i} \mathbf{C}^{-1} \frac{\partial \mathbf{C}}{\partial \theta_j} \right], \tag{11}$$

where T represents the vector transpose (Vogeley & Szalay 1996; Tegmark 1997; Tegmark, Taylor & Heavens 1997). In a simple case, in which galaxy shot noise n_{g}^{-1} is spatially homogeneous, and velocity noise $\sigma_{\text{u-noise}}$ is also constant, one can easily derive the following expression for a Fisher matrix (McDonald & Seljak 2009) by applying the formula to real and imaginary parts of the Fourier modes, $\delta_{\mathrm{g}}^{\mathrm{s}}(\boldsymbol{k})$ and $u^{\mathrm{s}}(\boldsymbol{k})$, in a periodic box of volume V:

$$F_{ij} = \frac{1}{2} V \int \frac{\mathrm{d}^3 k}{(2\pi)^3} \mathrm{tr} \left[\tilde{\Sigma}(\boldsymbol{k})^{-1} \frac{\partial \tilde{\Sigma}(\boldsymbol{k})}{\partial \theta_i} \tilde{\Sigma}(\boldsymbol{k})^{-1} \frac{\partial \tilde{\Sigma}(\boldsymbol{k})}{\partial \theta_j} \right], \tag{12}$$

where the summation over independent k modes is approximated by an integral $(1/2)V \int \mathrm{d}^3 x/(2\pi)^3$, and $\tilde{\Sigma}$ is a matrix of power spectra including noise terms of shot noise and velocity measurement error:

$$\tilde{\Sigma} \equiv \begin{pmatrix} P_{\mathrm{gg}}^{\mathrm{s}}(\boldsymbol{k}) + n_{\mathrm{g}}^{-1} & P_{\mathrm{gu}}^{\mathrm{s}}(\boldsymbol{k}) \\ P_{\mathrm{ug}}^{\mathrm{s}}(\boldsymbol{k}) & P_{\mathrm{uu}}^{\mathrm{s}}(\boldsymbol{k}) + n_{\mathrm{u}}^{-1} \sigma_{\text{u-noise}}^2 \end{pmatrix}. \tag{13}$$

We allow the number density for shot noise n_{g} to differ from the number density of the velocity measurements n_{u}, because galaxies with peculiar velocity measurements are usually a subset of galaxies with redshift measurements ($n_{\mathrm{u}} < n_{\mathrm{g}}$); measuring peculiar velocity requires much higher signal-to-noise ratio in the observations.

In reality, the noise terms vary with distance as the observed galaxy number density decreases with distance due to the flux limit of observations, and the peculiar velocity error from standard candles increases linearly with distance. We assume that the velocity noise comes from random non-linear motions of rms $\sigma_* \sim 300\,\mathrm{km\,s^{-1}}$, and observational errors of rms σ_{uobs}, which originate from the intrinsic scatter in astrophysical relations used as distance indicators:

$$\sigma_{\text{u-noise}}^2 = \sigma_*^2 + \sigma_{\mathrm{uobs}}^2, \quad \sigma_{\mathrm{uobs}}(\boldsymbol{x}) = \epsilon H_0^{-1} |\boldsymbol{x}|, \tag{14}$$

where the fractional error ϵ is typically about 8 per cent for supernovae, and 20 per cent for the Tully–Fisher and the Fundamental Plane distance indicators. We assume that these noise terms can be determined directly from observations, and are therefore not a function of uncertain cosmological parameters θ_i.

It turns out that we can replace the volume V by a volume integral $\int \mathrm{d}^3 x$ under the 'classical approximation' (Hamilton 1997; Abramo 2012):

$$F_{ij} = \frac{1}{2} \int \frac{\mathrm{d}^3 x \mathrm{d}^3 k}{(2\pi)^3} \mathrm{tr} \left[\tilde{\Sigma}(\boldsymbol{k}, \boldsymbol{x})^{-1} \frac{\partial \tilde{\Sigma}}{\partial \theta_i} \tilde{\Sigma}(\boldsymbol{k}, \boldsymbol{x})^{-1} \frac{\partial \tilde{\Sigma}}{\partial \theta_j} \right], \tag{15}$$

where $\tilde{\Sigma}$ now depends on $\boldsymbol{x}$ through noise terms, $n_{\mathrm{g}}(\boldsymbol{x})$, $n_{\mathrm{u}}(\boldsymbol{x})$, and $\sigma_{\mathrm{uobs}}(\boldsymbol{x})$. This mixture of a wavenumber and a position seems odd because Fourier transformations of $\delta(\boldsymbol{x})$ and $u(\boldsymbol{x})$ do not leave $\boldsymbol{x}$ as an independent variable. We can imagine, however, dividing the volume V into subvolumes where noise terms are approximately constant, Fourier transforming the fields in each of the subvolume, and obtaining equation (12) in the subvolume. The sum of such subvolume Fisher matrices gives equation (15). This process can be justified only if the wavelength is much smaller than the size of the subvolume, because (a) Fourier transform may not be possible for wavelength larger than the size of the subvolume, and (b) the simple summation of 'sub-Fisher matrix' is correct only if the fields are uncorrelated between the subvolumes. Since long-wavelength modes break these conditions, the classical approximation is valid for wavelengths smaller than the scale of noise variation, which is in the order of survey size. This original discussion of the classical approximation by Hamilton (1997) for a single density field is generalized to multiple tracers by Abramo (2012). We summarize the mathematical derivation for equation (15) in Appendix B1.

For a single field of galaxy density, the Fisher matrix reduces to the well-known form (Tegmark 1997):

$$F_{ij}^{\text{gg-only}} = \frac{1}{2} \int \frac{\mathrm{d}^3 x \mathrm{d}^3 k}{(2\pi)^3} \frac{\partial P_{\mathrm{gg}}^{\mathrm{s}}}{\partial \theta_i} \frac{\partial P_{\mathrm{gg}}^{\mathrm{s}}}{\partial \theta_j} \left[P_{\mathrm{gg}}^{\mathrm{s}}(\boldsymbol{k}) + n_{\mathrm{g}}^{-1}(\boldsymbol{x}) \right]^{-1}. \tag{16}$$

The Fisher matrix of the peculiar velocity power spectrum has a similar form

$$F_{ij}^{\text{uu-only}} = \frac{1}{2} \int \frac{\mathrm{d}^3 x \mathrm{d}^3 k}{(2\pi)^3} \frac{\partial P_{\mathrm{uu}}^{\mathrm{s}}}{\partial \theta_i} \frac{\partial P_{\mathrm{uu}}^{\mathrm{s}}}{\partial \theta_j} \left[P_{\mathrm{uu}}^{\mathrm{s}} + n_{\mathrm{u}}^{-1} \sigma_{\mathrm{uobs}}^2 \right]^{-1}. \tag{17}$$

We also show results of the Fisher matrix of density–velocity cross-power only:

$$F_{ij}^{\text{cross-only}} = \int \frac{\mathrm{d}^3 x \mathrm{d}^3 k}{(2\pi)^3} \frac{\partial P_{\mathrm{gu}}^{\mathrm{s}}}{\partial \theta_i} \frac{\partial P_{\mathrm{gu}}^{\mathrm{s*}}}{\partial \theta_j} \times \left[(P_{\mathrm{gg}}^{\mathrm{s}} + n_{\mathrm{g}}^{-1})(P_{\mathrm{uu}}^{\mathrm{s}} + n_{\mathrm{u}}^{-1} \sigma_{\mathrm{uobs}}^2) + P_{\mathrm{gu}}^{\mathrm{s2}} \right]^{-1}. \tag{18}$$

See Appendix B3.2 for the covariance of the cross-power spectrum.

3.2 General results

Before we forecast cosmological constraints for specific surveys, we show general results for constant number density $n_{\mathrm{g}} = n_{\mathrm{u}} = \bar{n}$. We consider how the two-field Fisher matrix for galaxy density and peculiar velocity (equation 15) improves cosmological constraints compared to those from galaxy redshift only (equation 16), peculiar velocity only (equation 17), or cross-power only (equation 18).

The six-dimensional integral in the Fisher matrix reduces to a three-dimensional integral by symmetry. We numerically integrate the Fisher matrix up to wavenumber $k_{\max}$ and radius $r_{\max} = cH_0 z_{\max}$, which corresponds to redshift $z_{\max}$, where $c = 3.0 \times 10^5\,\mathrm{km\,s^{-1}}$ is the speed of light:

$$\int \mathrm{d}^3 x \mathrm{d}^3 k = 4\pi \Omega_{\mathrm{sky}} \int_0^{k_{\max}} \mathrm{d}k \int_0^{r_{\max}} \mathrm{d}r \int_0^1 \mathrm{d}\mu, \tag{19}$$

where Ω_{sky} is the steradian of the field of view; we use $\Omega_{\mathrm{sky}} = 4\pi$ in this section, but all results simply scale as $\Delta\theta \propto \Omega_{\mathrm{sky}}^{-1/2}$. We

Table 2. 1σ constraints on parameters for constant galaxy number density $\bar{n} = 0.01\,(h^{-1}\,\mathrm{Mpc})^{-3}$ from two-field, galaxy density only (RSD only), and velocity power spectrum only.

	Free parameters	Fractional uncertainties $\Delta\theta_i/\theta_i$ (per cent)									
		$k_{\rm max} = 0.1\,h\,\mathrm{Mpc}^{-1}$					$k_{\rm max} = 0.2\,h\,\mathrm{Mpc}^{-1}$				
	θ_i	$f\sigma_8$	β	$r_{\rm g}$	$\sigma_{\rm g}$	$\sigma_{\rm u}$	$f\sigma_8$	β	$r_{\rm g}$	$\sigma_{\rm g}$	$\sigma_{\rm u}$
Two field	$f\sigma_8$, β(linear)	2.4	2.1				1.8	1.9			
	$f\sigma_8$, β	2.5	2.2				1.8	2.0			
	$f\sigma_8$, β, $r_{\rm g}$	2.5	2.2	0.30			1.8	2.0	0.30		
	$f\sigma_8$, β, $\Omega_{\rm b}h^2$, $\Omega_{\rm c}h^2$, h, $n_{\rm s}$	8.0	2.2				2.2	2.0			
	$f\sigma_8$, β, $\sigma_{\rm g}$, $\sigma_{\rm u}$	3.3	2.9		65	14	2.4	2.4		9.6	4.6
	All	8.5	2.9	0.30	67	14	2.8	2.4	0.30	11	4.7
	All +*Planck* prior	3.4	2.9	0.30	65	14	2.4	2.4	0.30	9.9	4.6
RSD only	$f\sigma_8$, β	13.8	15.8				4.9	5.6			
	$f\sigma_8$, β, $\sigma_{\rm g}$	18.7	20.2		85.2		10.1	10.5		17.0	
	$f\sigma_8$, β, $r_{\rm g}$	136	134	189			48.4	47.7	67.3		
Velocity only	$f\sigma_8$	4.0					3.7				

integrate up to $k_{\rm max} = 0.2\,h\,\mathrm{Mpc}^{-1}$ and $z_{\rm max} = 0.1$ unless otherwise mentioned.

We use equations (7)–(9) for the power spectra in redshift space, with $P_{\rm mm}$, $P_{{\rm m}\theta}$, and $P_{\theta\theta}$ from the one-loop RPT. In this section, we set fiducial values, $b = 1$, $r_{\rm g} = 1$, $\sigma_{\rm g}/\sqrt{2} = 3\,h^{-1}\,\mathrm{Mpc}$, $\sigma_{\rm u} = 13\,h^{-1}\,\mathrm{Mpc}$ for the model power spectrum, and set noise terms using galaxy number density $\bar{n} = 0.01\,(h^{-1}\,\mathrm{Mpc})^{-3}$, 20 per cent observational velocity error, $\epsilon = 0.2$, and non-linear random velocity rms $\sigma_* = 300\,\mathrm{km\,s^{-1}}$. We use the ΛCDM cosmology for the fiducial value of the growth rate parameter $f = \Omega_{\rm m}^{0.55}$ (Linder 2005), but we do not assume this relation between f and $\Omega_{\rm m}$ in the derivatives in the Fisher matrix, because we constrain possible deviation of $f\sigma_8$ from the ΛCDM cosmology. In the following subsections, we present the results of the Fisher matrix analysis for different subsets of cosmological parameters. We summarize the results in Table 2.

3.2.1 *Two free parameters: $f\sigma_8$ and β*

We first show results for two parameters $\boldsymbol{\theta} = (f\sigma_8, \beta)$, assuming other parameters are exactly known. Because f, σ_8, and b are completely degenerate, giving an uninvertible Fisher matrix, we have to select two combinations of three variables. For the fiducial set-up, the constraint on the growth rate $f\sigma_8$ from the two-field Fisher matrix is 1.8 per cent, while the constraint from redshift-space distortion only ($P^{\rm s}_{\rm gg}$ only) is 4.9 per cent. Adding peculiar velocity therefore improves the constraint by more than a factor of 2.

In Fig. 4, we show the 1σ constraints on $f\sigma_8$ and β as a function of $k_{\rm max}$. The figure shows that most of the constraints from velocity come from low $k \leq 0.1\,h\,\mathrm{Mpc}^{-1}$, while constraints from redshift-space distortion improves at large k. The velocity power spectrum damps by a factor k^{-2} faster than the galaxy power spectrum, and the measurement error is significant; these two factors make the signal-to-noise ratio of velocity decline very rapidly as k increases. In Fig. 5, we plot the same constraints as a function of $z_{\rm max}$, for $k_{\rm max} = 0.2\,h\,\mathrm{Mpc}^{-1}$. The constraint from two fields for $z_{\rm max} = 0.1$ are comparable to the constraint from redshift-space distortion for $z_{\rm max} = 0.2$, which has a volume of $1\,(h^{-1}\,\mathrm{Gpc})^3$.

In Fig. 6, we plot the constraints as a function of galaxy number density $\bar{n}$, for $k_{\rm max} = 0.2\,h\,\mathrm{Mpc}^{-1}$ and $z_{\rm max} = 0.1$. While constraints from redshift-space distortion alone reach the cosmic variance limit at $\bar{n} \sim 10^{-4}\,(h^{-1}\,\mathrm{Mpc})^3$, the constraints from two fields improve further with galaxy number density. Although the constraint on β is not limited by cosmic variance (at linear order with $r_{\rm g} = 1$), the constraint on $f\sigma_8$ is limited by the cosmic variance on the clustering amplitude of galaxies, $b\sigma_8$. The cosmic variance limit of $f\sigma_8$, however, is at the sub-per cent level because $b\sigma_8$ can be measured very precisely. The bottom panel illustrates that the constraint on β using both density and velocity is not limited by cosmic variance; the constraint continues to improve as number density increases, as the large number reduces the measurement error of velocity on average. The cancellation of cosmic variance is not perfect for non-linear power spectra because $P_{\rm mm}$, $P_{{\rm m}\theta}$, and $P_{\theta\theta}$ are not exactly equal to each other. However, the difference between linear and non-linear power spectra affects the Fisher matrix results only at very high number density, $\bar{n} \gtrsim 0.1\,(h^{-1}\,\mathrm{Mpc})^{-3}$, probably because signal-to-noise ratio is otherwise not good enough anyway

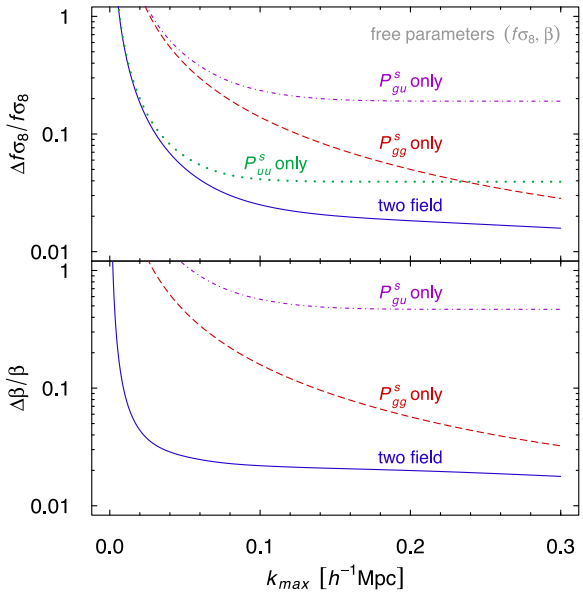

Figure 4. Constraints on $f\sigma_8$ (upper panel) and β (lower panel) as a function of $k_{\rm max}$ from galaxy density power spectrum only ('$P^{\rm s}_{\rm gg}$ only', red dashed lines), velocity power spectrum only ('$P^{\rm s}_{\rm uu}$ only', green dotted lines), density–velocity cross-power only ('$P^{\rm s}_{\rm gu}$ only', purple dash–dotted lines), and from both density and velocity field ('two field', blue solid lines). The galaxy number density is fixed to $\bar{n} = 10^{-2}\,(h^{-1}\,\mathrm{Mpc})^{-3}$. Parameters other than $f\sigma_8$ or β are fixed to their fiducial values, including $z_{\rm max} = 0.1$. The velocity power spectrum alone ($P^{\rm s}_{\rm uu}$) does not constrain β because it does not depend on galaxy bias.

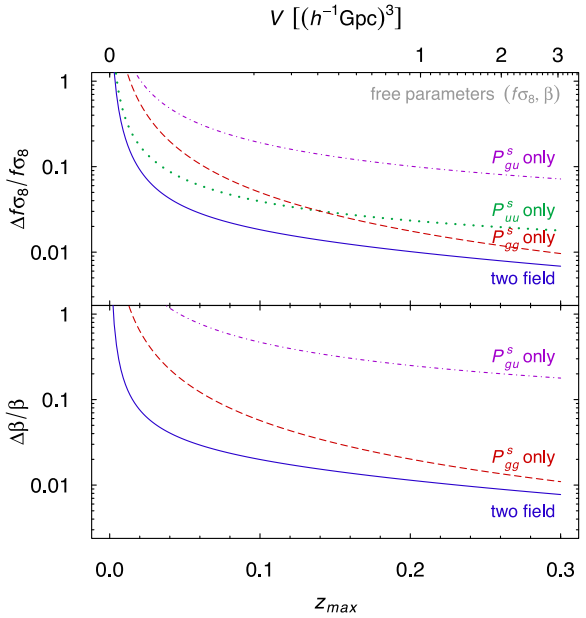

Figure 5. Same as Fig. 4, but as a function of $z_{\rm max}$ instead of $k_{\rm max}$. $k_{\rm max}$ is fixed to $0.2\,h\,{\rm Mpc}^{-1}$.

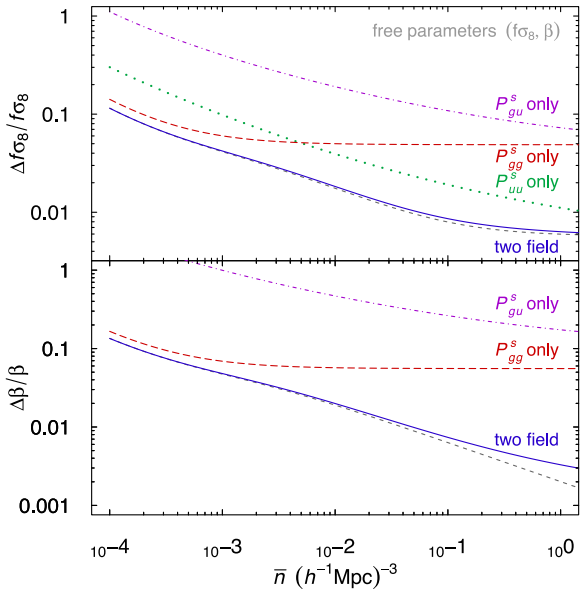

Figure 6. Constraints on $f\sigma_8$ (upper panel) and β (lower panel) as a function of galaxy number density ($\bar{n} = n_{\rm g} = n_{\rm u}$). See Fig. 4 for the description of lines. The short-dashed lines are results from two fields using linear theory; the one-loop RPT is used for other lines. Constraints on β from two fields continue to decrease, while the constraint from RSD only is limited by cosmic variance.

for $k \gtrsim 0.1\,h\,{\rm Mpc}^{-1}$, where the non-linearity makes the difference. In the figure, we plot the constraints using the linear power spectrum with the blue short dashed lines.

3.2.2 *Three free parameters: $f\sigma_8$, β, and ${\rm r_g}$*

From galaxy density alone, the growth rate $f\sigma_8$ and galaxy correlation coefficient $r_{\rm g}$ are highly degenerate. BT04 pointed out that peculiar velocity breaks this degeneracy and constrains $r_{\rm g}$ extremely well. Our result confirms this; the constraint on $f\sigma_8$ from the redshift survey weakens from 5 to 48 per cent, compared to the two-parameter case (Section 3.2.1), while two-field data constrains $r_{\rm g}$ to 0.3 per cent, and $f\sigma_8$ to the same precision as the two-parameter case. Peculiar velocity surveys can constrain growth rates, $f\sigma_8$ and β, equally well even if we add $r_{\rm g}$ as a free parameter.

3.2.3 *Four free parameters: $f\sigma_8$, β, $\sigma_{\rm g}$, and $\sigma_{\rm u}$*

Because the damping factor of the galaxy power spectrum, $\sigma_{\rm g}$, is affected by complicated non-linear pairwise velocity (e.g. Scoccimarro 2004), which depends on the galaxy population, $\sigma_{\rm g}$ is often treated as a nuisance parameter fitted against data. For the velocity damping factor, $\sigma_{\rm u}$, we do not yet have a theoretical model. Without knowing how it depends on cosmological parameters, we have to treat it as a free parameter as well. We investigate the effects of treating these damping factors as free parameters in this section. Because we know the order of magnitude of these parameters and know that they are positive, we add 100 per cent priors to the Fisher matrix:

$$F^{\sigma\ {\rm prior}}_{\sigma_{\rm g}\sigma_{\rm g}} = \sigma_{\rm g}^{-2}, \quad F^{\sigma\ {\rm prior}}_{\sigma_{\rm u}\sigma_{\rm u}} = \sigma_{\rm u}^{-2}. \tag{20}$$

The constraints on $f\sigma_8$ and β weaken by about 20–30 per cent, from 1.8 to 2.4 per cent on $f\sigma_8$, and from 2.0 to 2.4 per cent on β, respectively. The constraint from redshift-distortion alone also weakens from 5 to 10 per cent. We conclude that uncertainty in the damping parameter has a moderate, but not severe, effect on the forecast constraints.

3.2.4 *Free cosmological parameters*

Finally, we vary cosmological parameters, cold dark matter density $\Omega_{\rm c}h^2$, baryon density $\Omega_{\rm b}h^2$, Hubble constant h, and spectral index $n_{\rm s}$ in addition to $f\sigma_8$ and β. We take the derivative with respect to cosmological parameters numerically by generating power spectra with cosmological parameters changed by ± 1 per cent:

$$\frac{\partial P}{\partial \theta_i} \approx \frac{P(\theta_i + \Delta\theta_i) - P(\theta_i - \Delta\theta_i)}{2\Delta\theta_i}, \tag{21}$$

where $\Delta\theta_i = 0.01\theta_i$. The constraint on β is unaffected, because the relation between $\delta_{\rm g}$ and u only depends on β, not on other cosmological parameters in the linear order. The constraint on $f\sigma_8$ weakens from 1.8 to 2.2 per cent.

Since cosmological parameters are well constrained by the CMB, we add the prior expected from the *Planck* observation (Planck Collaboration 2013). We use the forecast for the full *Planck* mission by Perotto et al. (2006); we calculate the covariance matrix of $\Omega_{\rm c}h^2$, $\Omega_{\rm b}h^2$, h, and $n_{\rm s}$, marginalized over the other parameters, using their publicly available Markov chain Monte Carlo data.[4] We add the inverse of the covariance matrix to the Fisher matrix as an independent prior from *Planck*. We do not add a prior on f or σ_8 from the CMB, because model-dependent extrapolation to $z = 0$ is necessary for such constraints. The *Planck* priors marginalized for each parameter are $\Delta\Omega_{\rm b}h^2 = 0.00022$, $\Delta\Omega_{\rm c}h^2 = 0.0024$, $\Delta h = 0.017$, and $\Delta n_{\rm s} = 0.0074$.

After adding the *Planck* prior, the constraints on $f\sigma_8$ and β recover the two-parameter constraint. We also vary all nine parameters, $\boldsymbol{\theta} = (f\sigma_8, \beta, r_{\rm g}, \sigma_{\rm g}, \sigma_{\rm u}, \Omega_{\rm c}h^2, \Omega_{\rm b}h^2, h, n_{\rm s})$, with the *Planck* prior. The result is same as the four-parameter constraint with $f\sigma_8$, β, $\sigma_{\rm g}$, and $\sigma_{\rm u}$. With the precise measurement from the CMB, the shape

[4] lesgourg.web.cern.ch/lesgourg/codes/chains_0606227.html

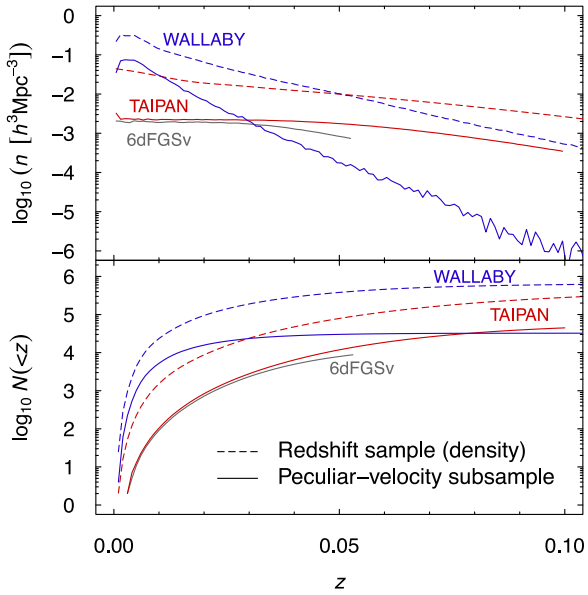

Figure 7. Number density (upper panel) and cumulative number (lower panel) of galaxies for the 6dF Galaxy Survey velocity subsample (6dFGSv, grey line), TAIPAN survey (red lines), and WALLABY+WNSHS survey (blue lines). Dashed lines are for the redshift (density only) samples, and solid lines are for the peculiar velocity subsamples.

of the power spectrum is no longer a source of uncertainty in the growth rate.

We have presented the results of the two-field Fisher matrix analysis for galaxy density and peculiar velocity, comparing with those for a single field with density or velocity only. Peculiar velocity measurements improve the measurements for more than a factor of 2 compared to density alone for $\bar{n} = 10^{-2}\,(h^{-1}\,\mathrm{Mpc})^{-3}$, and improve even more as we increase the number density, without the cosmic variance limit. The non-linear power spectrum with RPT does not alter the Fisher matrix results significantly compared to the linear power spectrum. The uncertainty in the redshift-space damping parameters, σ_g and σ_u, degrade the constraints by 20–30 per cent, which can be improved by future theoretical work.

4 FORECASTING FUTURE PECULIAR VELOCITY SURVEYS

We apply our Fisher matrix of galaxy density and peculiar velocity to existing and future peculiar velocity surveys. In Section 4.1, we first review the measurements from the existing 6dF Galaxy Survey (6dFGS), and the Fisher matrix forecast by BT04 for the 6dF survey, and compare them with our calculations. We then present the forecasts for the future surveys in Sections 4.2 and 4.3. We use distance-dependent galaxy numbers, galaxy bias b, and sky coverage Ω_sky expected for each of the surveys, which we describe in the following sections. Other parameters in the Fisher matrix are the same as those in Section 3.2. In Fig. 7, we plot the expected galaxy number densities with redshift measurement, n_g, and with additional peculiar velocity measurement, n_u. We summarize the results in Table 3.

4.1 6dF Galaxy Survey

The 6dFGS is a low-redshift survey of early-type galaxies out to $z \lesssim 0.15$, covering 17 046 deg^2 in the southern sky, and containing 136 304 redshifts (Jones et al. 2004, 2009). The velocity subsample (6dFGSv) contains 8885 galaxies in the redshift range $z \leq 0.05$, with peculiar velocities measured through the Fundamental Plane relation (Magoulas et al. 2012). The redshift survey measured the growth rate through the redshift-space distortions with 13 per cent precision at effective redshift of 0.067 ($f\sigma_8 = 0.423 \pm 0.053$; Beutler et al. 2012). Their Fisher matrix calculation gives constraints on $f\sigma_8$ of 23 per cent for $k_\mathrm{max} = 0.1\,h\,\mathrm{Mpc}^{-1}$, and 8.3 per cent for $k_\mathrm{max} = 0.2\,h\,\mathrm{Mpc}^{-1}$, consistent with their actual analysis (all values for wavenumbers k are in units of $h\,\mathrm{Mpc}^{-1}$, hereafter). The velocity subsample combined with the reconstructed velocity field from a full-sky density field measures β with about 25 per cent precision (Magoulas et al., in preparation).

In order to determine the redshift distribution of galaxies, we use 125 random mocks of the 6dFGS velocity subsample, each of which contains 8986 galaxies (We recently removed 90 objects from the subsample, which have problems with photometry or spectroscopy. The number we use here is that before the removal.) We require the J-band luminosity $J \leq 13.65$, and velocity dispersion to be larger than $116\,\mathrm{km\,s}^{-1}$ (see Magoulas et al. 2012, for the details about the mock sample). Velocity subsample is limited to $z_\mathrm{max} = 0.055$ because the velocity dispersion measurements for the Fundamental Plane relation become dominated by systematics beyond that redshift with the 6dF spectrograph. Because the Fisher matrix analysis for the redshift sample is already discussed in Beutler et al. (2012), we only consider the velocity subsample in this paper, $n_\mathrm{g} = n_\mathrm{u}$. The field of view is the southern half of the sky, excluding the Galactic plane (Galactic latitude $|b| < 10^\circ$), which is $\Omega_\mathrm{sky} = 1.65\pi$ sr. We set galaxy bias to $b = 1.4$ (Beutler et al. 2012), and fractional velocity measurement error to $\epsilon = 0.25$.

Our Fisher matrix calculation with two free parameters ($f\sigma_8$ and β) gives 16 per cent for $k_\mathrm{max} = 0.1$, and 13 per cent for $k_\mathrm{max} = 0.2$, respectively, on the uncertainty of β. This is in the same order as the peculiar velocity analysis by Magoulas et al. (in preparation), but we cannot compare our Fisher matrix results directly with their analysis, because our Fisher matrix results are the combined constraints from redshift-space distortions and the velocity measurements, while the velocity–velocity analysis uses the density to construct the model velocity, but is not combined with the redshift-space distortion analysis for the density.

BT04, on the other hand, predicted a precision of 5 per cent for the 6dFGS from redshift-space distortion alone, and 2 per cent from the two-field Fisher matrix for density and velocity. Both of these forecasts are much smaller than the results of the 6dF survey, including the Fisher matrix calculation in Beutler et al. (2012). Details, such as cosmological parameters or power spectrum model, cannot explain the difference. One possibility is that they might have used an order of magnitude larger number density, even though their estimates of the total galaxy number, about 10^5 redshifts and about 15 000 velocity measurements, are roughly correct; their equation (29) relates total number for galaxies N_g to number density (number of galaxies per unit volume), but the actual integral of the equation gives $4\pi N_\mathrm{g}$ in total, which means that the number density could be 4π larger than it should be. If this were true, it would explain why their forecast is closer to our forecast for Widefield ASKAP L-band Legacy All-sky Blind Survey (WALLABY) rather than for 6dFGS.

4.2 TAIPAN survey

Transforming Astronomical Imaging surveys through Polychromatic Analysis of Nebulae (TAIPAN) survey is a planned future successor of the 6dFGS using the UK Schmidt Telescope with

Table 3. A Fisher matrix forecast for fractional uncertainties of parameters $\Delta\theta_i/\theta_i$, including constraints on growth factors $f\sigma_8$ and β from the two-field Fisher matrix of galaxy density and peculiar velocity, galaxy density only ('RSD only'), and velocity only ('P_{uu}'). The upper block of numbers are for $k_{max} = 0.1\,h\,\mathrm{Mpc}^{-1}$, and the lower block is for $k_{max} = 0.2\,h\,\mathrm{Mpc}^{-1}$.

Survey	Free parameters	Fractional uncertainties $\Delta\theta_i/\theta_i$ (per cent)									
		Two fields					RSD only				P_{uu}
	θ_i	$f\sigma_8$	β	r_g	σ_g	σ_u	$f\sigma_8$	β	r_g	σ_g	$f\sigma_8$
6dFGSv	$f\sigma_8, \beta$	15	16								25
	$f\sigma_8, \beta, r_g$	15	16	4.2							
	$f\sigma_8, \beta, \sigma_g, \sigma_u$	18	19		96	66					
TAIPAN	$f\sigma_8, \beta$	7.1	7.4				28	31			14
	$f\sigma_8, \beta, r_g$	7.1	7.4	0.87			370	360	47		
	$f\sigma_8, \beta, \sigma_g, \sigma_u$	8.9	9.1		33	36	92				
WALLABY+WNSHS	$f\sigma_8, \beta$ (linear)	3.5	3.8				11	13			13
	$f\sigma_8, \beta$	4.3	4.8				11	13			13
	$f\sigma_8, \beta, r_g$	4.4	4.8	0.29			80	78	120		
	$f\sigma_8, \beta, \sigma_g, \sigma_u$	6.0	6.4		70	23	14	16	85	79	
	All +*Planck* prior	6.1	6.4	0.29	70	23	81	80	120		
											($k_{max} = 0.1\,h\,\mathrm{Mpc}^{-1}$)
6dFGSv	$f\sigma_8, \beta$	12	13								24
	$f\sigma_8, \beta, r_g$	12	13	4.2							
	$f\sigma_8, \beta, \sigma_g, \sigma_u$	15	16		43	66					
TAIPAN	$f\sigma_8, \beta$	5.6	6.2				10	11			14
	$f\sigma_8, \beta, r_g$	5.6	6.1	0.87			130	130	170		
	$f\sigma_8, \beta, \sigma_g, \sigma_u,$	7.5	7.6		16	17	33	37	93		
WALLABY+WNSHS	$f\sigma_8, \beta$ (linear)	2.6	3.0				4.3	5.2			11
	$f\sigma_8, \beta$	3.0	3.6				4.3	5.2			11
	$f\sigma_8, \beta, r_g$	3.0	3.6	0.29			32	31	50		
	$f\sigma_8, \beta, \sigma_g, \sigma_u,$	4.5	4.7		13	7.0	8.3	8.9	18		
	All +*Planck* prior	4.6	4.8	0.29	14	7.0	34	33	50	20	
											($k_{max} = 0.2\,h\,\mathrm{Mpc}^{-1}$)

upgraded fibres. The new spectrograph improves the velocity dispersion measurements, which allows us to extend the upper limit of the velocity subsample from 0.055 for 6dFGSv to 0.1, and to increase the number density by decreasing the lower bound of the velocity dispersion from 116 km s^{-1} for 6dFGSv to 70 km s^{-1}.

We generated 125 mock Fundamental Plane galaxies for TAIPAN, similar to those for the 6dFGSv, to estimate the number of observed galaxies. We assume peculiar velocity measurements are available for J-band magnitude brighter than 15.15, and velocity dispersion larger than 70 km s^{-1} up to $z = 0.1$. We estimate the total number of velocity sample to be about 45 000. The number of redshifts in the sample increases by about a factor of 4 compared to 6dFGS, out to $z \sim 0.2$, assuming an r-band magnitude limit of 17. We assume a galaxy bias $b = 1.4$, same as for 6dFGS, and a fractional velocity error $\epsilon = 0.2$.

The TAIPAN survey can constrain $f\sigma_8$ to 7.1 per cent ($k_{max} = 0.1$) or 5.6 per cent ($k_{max} = 0.2$) if the damping constants, σ_g and σ_u, are known, or 8.9 per cent ($k_{max} = 0.1$) to 7.5 per cent ($k_{max} = 0.2$) if they are unknown nuisance parameters. Therefore the constraints from the TAIPAN survey are expected to be a factor of 2 better than those from the 6dFGSv. We will also show in Section 4.4 that TAIPAN will be able to put interesting constraints on k-dependent growth rates.

4.3 The WALLABY and the WNSHS surveys

WALLABY[5] is a planned H I survey with the Australian SKA Pathfinder (ASKAP), covering 3π sr of sky (Johnston et al. 2008; Duffy et al. 2012, and references therein). A similar survey, The Westerbork Northern Sky H I Survey (WNSHS),[6] is planned in the other π sr in the Northern hemisphere using Aperture Tile in Focus (APERTIF) on the Westerbork Synthesis Radio Telescope. For simplicity, we assume that both surveys will have the predicted WALLABY rms of 1.6 mJy in a channel of width 3.9 km s^{-1}. WNSHS may be somewhat deeper in practice. This results in a 5σ (velocity integrated) redshift catalogue of $\sim$0.8 million objects (Duffy et al. 2012). For Tully–Fisher velocities, additional constraints of width >80 km s^{-1}, inclination $>30^\circ$, and 3σ per channel result in a reduced mock catalogue of $\sim$32 000 galaxies.

We assume galaxy bias $b = 0.7$ following Beutler et al. (2012), which is based on measurements from the H I Parkes All-Sky Survey (Basilakos et al. 2007). The fractional velocity error is set to $\epsilon = 0.2$. Our Fisher matrix forecast for this all-sky H I is 3.0 per cent for $f\sigma_8$, and 3.6 per cent for β, for $k_{max} = 0.2$, if we know the values of damping constants σ_g and σ_u. The non-linear effect slightly weakens the constraint; the forecasts using the linear power spectra are 2.6 per cent for $f\sigma_8$ and 3.0 per cent for β, respectively. If we marginalize over damping constants, the constraints degrade by 30–50 per cent. Compared to redshift measurements alone, adding peculiar velocity data reduces the uncertainties by about 40 per cent. The galaxy correlation coefficient r_g can be constrained to 0.3 per cent.

Beutler et al. (2012) have forecast constraints on the growth rate $f\sigma_8$ from redshift-space distortion alone: 10.5 per cent for $k = 0.1$, and 3.9 per cent for $k = 0.2$, respectively. Our forecasts are

[5] http://www.atnf.csiro.au/research/WALLABY

[6] http://www.astron.nl/jozsa/wnshs

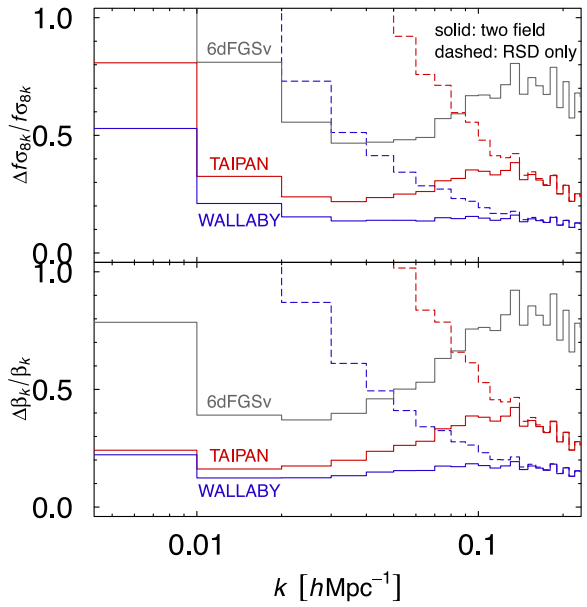

Figure 8. Constraints on $f\sigma_8$ and β as a function of wavenumber k, in bins of widths $\Delta k = 0.01\,h\,\mathrm{Mpc}^{-1}$. See Fig. 7 for line types and colours. Peculiar velocity surveys improve the constraints in k bins for $k \leq 0.1\,h\,\mathrm{Mpc}^{-1}$, because they are not limited by the cosmic variance. k-dependence constrains modified theories of gravity that have scale-dependent growth rates.

consistent with these results, although slightly larger for $k = 0.2$. They also reported that the multiple-tracer method (McDonald & Seljak 2009) between early-type galaxies from TAIPAN survey and gas-rich galaxies from the WALLABY survey in the overlap volume does not improve the constraints, giving almost the same constraint as WALLABY+WNSHS only. This is because the number density for TAIPAN is not large enough to make the multiple biased-tracer method effective. The method works best when both of the galaxy populations have high number densities, and simultaneously have a large difference in their bias, which is a difficult condition to satisfy. The advantage of the peculiar velocity survey is that two tracers (density and velocity) are available with high densities, only limited by the condition that the Tully–Fisher relation holds.

4.4 Constraining k dependence

Measuring growth rates, $f\sigma_8$ or β on different scales, as a function of wavenumber k for example, is an independent test of general relativity on cosmological scales. General relativity predicts that these growth rates are functions of time only, independent of the wavenumber, but other theories of gravity can have k-dependent growth rates. The growth rate β can also be scale dependent at large scales if non-Gaussian initial conditions introduce scale-dependent bias. In Fig. 8, we show constraints on the growth rates in bins of width $\Delta k = 0.01\,h\,\mathrm{Mpc}^{-1}$. We integrate the Fisher matrix with two free parameters, $f\sigma_8$ and β, in wavenumber ranges $n\Delta k$ to $(n + 1)\Delta k$ for $n = 0, 1, 2, \ldots$. The multi-tracer approach with density and velocity improves the constraints on β at large scales. The TAIPAN survey can measure growth rates, β and $f\sigma_8$, to 20–30 per cent in each bin, and the WALLABY+WNSHS surveys produce measurements with about 15 per cent precision in each bin. One caveat is that the classical approximation in the Fisher matrix could break down, giving inaccurate forecasts, at low k comparable to the size of the surveys; we leave the work beyond classical approximation to future studies. The two-field constraints on growth rates predict large improvements for $k \leq 0.1\,h\,\mathrm{Mpc}^{-1}$ by evading the cosmic variance limit. These are the ranges where we can recognize possible deviations from the ΛCDM model, distinguishing them from non-linear dynamics, non-linear redshift-space distortions, or scale-dependent galaxy bias.

5 SUMMARY AND DISCUSSION

We summarize our conclusions as follows.

(i) We have improved the model for the auto- and cross-power spectra of galaxy density contrast and line-of-sight peculiar velocity fields. We show that the density–velocity cross-power spectrum and the velocity autopower spectrum contain strong redshift-space distortions. We introduce a new damping term to the model equations, which needs to be considered in future velocity analyses to avoid biased results.

(ii) We compare the model equations for the power spectra with the GiggleZ simulation using the subhaloes. We calibrate the nearest particle method to compute reliable velocity power spectra (Appendix A). The comparison shows that our model agrees well with the simulation for $k \lesssim 0.2\,h\,\mathrm{Mpc}^{-1}$.

(iii) We derive the Fisher matrix formula for multiple correlated fields when the noise terms vary with distance, including a pair of galaxy density and velocity fields whose shot noise and velocity measurement error increase with distance (Appendix B1). The derivation reminds us that the Fisher matrix uses the classical approximation which breaks down at low k. Since much of the constraint from peculiar velocity comes from low k, it is worthwhile to re-examine the validity of the classical approximation for peculiar velocities in the future. We also derive an equivalent Fisher matrix formula written in terms of the covariance of power spectra estimators (Appendix B3).

(iv) When the number density of the peculiar velocity sample is the same as the redshift sample, $n_\mathrm{u} = n_\mathrm{g}$, the peculiar velocity survey improves the constraints on growth rates, $f\sigma_8$ and β by more than a factor of 2 at $k_\mathrm{max} = 0.2\,h\,\mathrm{Mpc}^{-1}$ and about a factor of 5 for $k_\mathrm{max} = 0.1\,h\,\mathrm{Mpc}^{-1}$ for redshifts less than 0.1 (Section 3.2). Peculiar velocity surveys can also measure the galaxy–matter cross-correlation coefficient r_g very precisely. With redshift-space distortions alone, in contrast, $f\sigma_8$ and r_g are highly degenerate, weakening the constraint by an order of magnitude if r_g is a free parameter.

(v) Lack of knowledge of the damping constants of redshift-space distortions, σ_g and σ_u, degrade the constraint on $f\sigma_8$ by about 50 per cent, e.g. from 3 to 4.5 per cent for the forecast for the WALLABY survey. Further development of the theory of velocity power spectrum in redshift space is necessary to extract accurate parameters from future peculiar velocity surveys. Uncertainties in the other cosmological parameters do not affect the constraints on the growth rates when the *Planck* CMB data are added.

(vi) Future peculiar velocity surveys, TAIPAN, WALLABY, and WNSHS, will constrain the growth rate $f\sigma_8$ with 3 per cent precision at low redshift $z \leq 0.05$. The growth rate can also be measured at different scales. In wavenumber bins with width $\Delta k = 0.01\,h\,\mathrm{Mpc}^{-1}$, $f\sigma_8$ and β can be measured to 20–30 per cent by the TAIPAN survey, and about 15 per cent by the WALLABY+WNSHS surveys in the range $0.01 \leq k \leq 0.1\,h\,\mathrm{Mpc}^{-1}$. These constraints on very large scales are largely improved, compared to redshift measurements alone, by the strength of peculiar velocity surveys that cosmic variance is not a fundamental limit. We can use the physical relation between

the measured density and velocity to measure the growth rate β. These strong constraints contribute to constraining dark energy and modified gravity, which can have various growth rate functions of time and scale.

We show that peculiar velocity surveys provide competitive growth rate measurements at low redshift, $z \lesssim 0.1$. Future peculiar velocity surveys measure both redshifts and velocities with high number densities. Their biggest strength is in measuring the growth rate as a function of scale, which provides independent constraints on dark energy and modified theories of gravity. These features of low redshift and scale dependence are complimentary to large high-redshift surveys which measure growth rates as a function of time.

ACKNOWLEDGEMENTS

We thank Takahiko Matsubara, Wojciech Hellwing, Teppei Okumura, and Maciej Bilicki for useful discussions, and an anonymous referee for a careful reading of our paper and helpful comments. This research was conducted by the Australian Research Council Centre of Excellence for All-sky Astrophysics (CAASTRO), through project number CE110001020. We acknowledge the support of the Australian Research Council through Future Fellowship awards, FT110100639 (CB) and FT100100595 (TD). GBP acknowledges support from S. Wyithe's ARC Laureate grant (FL110100072).

REFERENCES

Abate A., Erdoğdu P., 2009, MNRAS, 400, 1541
Abramo L. R., 2012, MNRAS, 420, 2042
Adshead P., Baxter E. J., Dodelson S., Lidz A., 2012, Phys. Rev. D, 86, 063526
Amendola L. et al., 2013a, Living Rev. Relativ., 16, 6
Amendola L., Kunz M., Motta M., Saltas I. D., Sawicki I., 2013b, Phys. Rev. D, 87, 023501
Asaba S., Hikage C., Koyama K., Zhao G.-B., Hojjati A., Pogosian L., 2013, J. Cosmol. Astropart. Phys., 8, 29
Ballinger W. E., Peacock J. A., Heavens A. F., 1996, MNRAS, 282, 877
Basilakos S., Plionis M., Kovač K., Voglis N., 2007, MNRAS, 378, 301
Bernardeau F., van de Weygaert R., 1996, MNRAS, 279, 693
Bernardeau F., Colombi S., Gaztañaga E., Scoccimarro R., 2002, Phys. Rep., 367, 1
Bernstein G. M., Cai Y.-C., 2011, MNRAS, 416, 3009
Beutler F. et al., 2012, MNRAS, 423, 3430
Blake C. et al., 2011, MNRAS, 415, 2876
Branchini E. et al., 2001, MNRAS, 326, 1191
Branchini E., Eldar A., Nusser A., 2002, MNRAS, 335, 53
Burkey D., Taylor A. N., 2004, MNRAS, 347, 255 (BT04)
Carlson J., White M., Padmanabhan N., 2009, Phys. Rev. D, 80, 043531
Cautun M. C., van de Weygaert R., 2011, Astrophysics Source Code Library, The DTFE Public Software: The Delaunay Tessellation Field Estimator Code, preprint (arXiv:1105.0370)
Crocce M., Scoccimarro R., 2006, Phys. Rev. D, 73, 063519
Dalal N., Doré O., Huterer D., Shirokov A., 2008, Phys. Rev. D, 77, 123514
D'Aloisio A., Zhang J., Jeong D., Shapiro P. R., 2013, MNRAS, 428, 2765
Davis M., Nusser A., Willick J. A., 1996, ApJ, 473, 22
Davis M., Nusser A., Masters K. L., Springob C., Huchra J. P., Lemson G., 2011, MNRAS, 413, 2906
Dekel A., Lahav O., 1999, ApJ, 520, 24
de la Torre S., Guzzo L., 2012, MNRAS, 427, 327
de la Torre S. et al., 2013, A&A, 557, A54
de Putter R., Doré O., Takada M., 2013, preprint (arXiv:1308.6070)
Desjacques V., Sheth R. K., 2010, Phys. Rev. D, 81, 023526
Desjacques V., Seljak U., Iliev I. T., 2009, MNRAS, 396, 85
Duffy A. R., Meyer M. J., Staveley-Smith L., Bernyk M., Croton D. J., Koribalski B. S., Gerstmann D., Westerlund S., 2012, MNRAS, 426, 3385
Elia A., Ludlow A. D., Porciani C., 2012, MNRAS, 421, 3472
Erdoğdu P. et al., 2006, MNRAS, 373, 45
Feindt U. et al., 2013, A&A, 560, 90
Feldman H. A., Kaiser N., Peacock J. A., 1994, ApJ, 426, 23
Feldman H. A., Watkins R., Hudson M. J., 2010, MNRAS, 407, 2328
Gil-Marín H., Wagner C., Verde L., Jimenez R., Heavens A. F., 2010, MNRAS, 407, 772
Guzzo L. et al., 2008, Nature, 451, 541
Hamaus N., Seljak U., Desjacques V., 2011, Phys. Rev. D, 84, 083509
Hamilton A. J. S., 1997, MNRAS, 289, 285
Hand N. et al., 2012, Phys. Rev. Lett., 109, 041101
Hockney R. W., Eastwood J. W., 1988, Computer Simulation Using Particles. Taylor & Francis, Bristol, PA
Hudson M. J., Turnbull S. J., 2012, ApJ, 751, L30
Ishikawa T., Totani T., Nishimichi T., Takahashi R., Yoshida N., Tonegawa M., 2014, MNRAS, 443, 3359
Jaffe A. H., Kaiser N., 1995, ApJ, 455, 26
Jennings E., 2012, MNRAS, 427, L25
Jennings E., Baugh C. M., Li B., Zhao G.-B., Koyama K., 2012, MNRAS, 425, 2128
Jeong D., Komatsu E., 2006, ApJ, 651, 619
Jing Y. P., 2005, ApJ, 620, 559
Johnson A. et al., 2014, MNRAS, 444, 3926
Johnston S. et al., 2008, Exp. Astron., 22, 151
Jones D. H. et al., 2004, MNRAS, 355, 747
Jones D. H. et al., 2009, MNRAS, 399, 683
Kaiser N., 1987, MNRAS, 227, 1
Kaiser N., 1988, MNRAS, 231, 149
Kitaura F. S., Enßlin T. A., 2008, MNRAS, 389, 497
Kitaura F.-S., Angulo R. E., Hoffman Y., Gottlöber S., 2012, MNRAS, 425, 2422
Kwan J., Lewis G. F., Linder E. V., 2012, ApJ, 748, 78
Lavaux G., Tully R. B., Mohayaee R., Colombi S., 2010, ApJ, 709, 483
Lavaux G., Afshordi N., Hudson M. J., 2013, MNRAS, 430, 1617
Lewis A., Challinor A., Lasenby A., 2000, ApJ, 538, 473
Linder E. V., 2005, Phys. Rev. D, 72, 043529
Ma Y.-Z., Scott D., 2013, MNRAS, 428, 2017
Ma Y.-Z., Branchini E., Scott D., 2012, MNRAS, 425, 2880
Ma Y.-Z., Taylor J. E., Scott D., 2013, MNRAS, 436, 2029
Macaulay E., Feldman H., Ferreira P. G., Hudson M. J., Watkins R., 2011, MNRAS, 414, 621
McDonald P., Seljak U., 2009, J. Cosmol. Astropart. Phys., 10, 7
Magoulas C. et al., 2012, MNRAS, 427, 245
Mao Y., Shapiro P. R., Mellema G., Iliev I. T., Koda J., Ahn K., 2012, MNRAS, 422, 926
Matarrese S., Verde L., 2008, ApJ, 677, L77
Nishimichi T., Taruya A., 2011, Phys. Rev. D, 84, 043526
Nusser A., Davis M., 1994, ApJ, 421, L1
Nusser A., Davis M., 2011, ApJ, 736, 93
Okumura T., Seljak U., Desjacques V., 2012, J. Cosmol. Astropart. Phys., 11, 14
Peacock J. A., Dodds S. J., 1994, MNRAS, 267, 1020
Peacock J. A. et al., 2001, Nature, 410, 169
Perotto L., Lesgourgues J., Hannestad S., Tu H., Wong Y. Y., 2006, J. Cosmol. Astropart. Phys., 10, 13
Planck Collaboration, 2013, preprint (arXiv:1303.5076)
Pueblas S., Scoccimarro R., 2009, Phys. Rev. D, 80, 043504
Samushia L. et al., 2013, MNRAS, 429, 1514
Schaap W. E., van de Weygaert R., 2000, A&A, 363, L29
Scoccimarro R., 2004, Phys. Rev. D, 70, 083007
Seljak U., 2009, Phys. Rev. Lett., 102, 021302
Slosar A., Hirata C., Seljak U., Ho S., Padmanabhan N., 2008, J. Cosmol. Astropart. Phys., 8, 31
Smith R. E. et al., 2003, MNRAS, 341, 1311
Song Y.-S., Percival W. J., 2009, J. Cosmol. Astropart. Phys., 10, 4

Springel V., 2005, MNRAS, 364, 1105
Springel V., White S. D. M., Tormen G., Kauffmann G., 2001, MNRAS, 328, 726
Springob C. M., Masters K. L., Haynes M. P., Giovanelli R., Marinoni C., 2007, ApJS, 172, 599
Strauss M. A., Willick J. A., 1995, Phys. Rep., 261, 271
Sunyaev R. A., Zeldovich I. B., 1980, MNRAS, 190, 413
Takahashi R., Sato M., Nishimichi T., Taruya A., Oguri M., 2012, ApJ, 761, 152
Taruya A., Koyama K., Hiramatsu T., Oka A., 2014, Phys. Rev. D, 89, 3509
Tegmark M., 1997, Phys. Rev. Lett., 79, 3806
Tegmark M., Taylor A. N., Heavens A. F., 1997, ApJ, 480, 22
Tegmark M., Hamilton A. J. S., Strauss M. A., Vogeley M. S., Szalay A. S., 1998, ApJ, 499, 555
Tegmark M. et al., 2004, Phys. Rev. D, 69, 103501
Turnbull S. J., Hudson M. J., Feldman H. A., Hicken M., Kirshner R. P., Watkins R., 2012, MNRAS, 420, 447
Vogeley M. S., Szalay A. S., 1996, ApJ, 465, 34
Watkins R., Feldman H. A., Hudson M. J., 2009, MNRAS, 392, 743
Weinberg D. H., Mortonson M. J., Eisenstein D. J., Hirata C., Riess A. G., Rozo E., 2013, Phys. Rep., 530, 87
White M., Song Y.-S., Percival W. J., 2009, MNRAS, 397, 1348
Zheng Y., Zhang P., Jing Y., Lin W., Pan J., 2013, Phys. Rev. D, 88, 3510

APPENDIX A: NEAREST PARTICLE METHOD FOR VELOCITY POWER SPECTRUM

We calculate the auto- and cross-power spectra of subhalo density and peculiar velocity by Fourier transforming the density and velocity fields assigned on regular grid points. In this appendix, we explain how we calculate the discrete fields and correct for the smoothing and aliasing due to finite grid points. The goal is to minimize the numerical effect that depends on the grid resolution. We first review the procedure for the density field by Jing (2005) in Section A1, and then explain an analogous procedure for the velocity field in Section A2.

Let us consider N particles in a periodic box of length L on a side, at positions $\boldsymbol{x}_p$, with line-of-sight velocity u_p for $p = 1, \ldots, N$. We sample discrete densities and velocities on $N_{\rm grid}^3$ regular grid points at $\boldsymbol{x}_I$ for $I = 1, \ldots, N_{\rm grid}^3$.

A1 Density power spectrum

We use the standard CIC method to calculate the density field (Hockney & Eastwood 1988). The power spectrum calculated from this discrete density grid is well understood. We summarize the procedure by Jing (2005). The number density field before sampling is a sum of Dirac delta functions $\delta_{\rm D}$,

$$n(x) = \sum_{p=1}^{N} \delta_{\rm D}(\boldsymbol{x} - \boldsymbol{x}_p). \tag{A1}$$

This is the density field independent of gridding. The density field sampled on a grid point $\boldsymbol{x}_I$ becomes

$$\tilde{n}(x_I) = \int {\rm d}^3 y \; W_{\rm g}(\boldsymbol{x}_I - \boldsymbol{y}) n(y), \tag{A2}$$

where the window function $W_{\rm g}$ for CIC is

$$W_{\rm g}(\boldsymbol{r}) = \prod_{i=1}^{3} (1 - |r_i|/\Delta x), \tag{A3}$$

if $|r_i| \le \Delta x \equiv L/N_{\rm grid}$ for all $i = 1, 2, 3$, and zero otherwise. The galaxy (subhalo) autopower spectrum calculated from the grid $\tilde{P}_{\rm gg}$ is related to the true power spectrum $P_{\rm gg}$ in the following way:

$$\tilde{P}_{\rm gg}(\boldsymbol{k}) = \sum_{\boldsymbol{n}} |\hat{W}_{\rm g}(\boldsymbol{k} + k_P \boldsymbol{n})|^2 P_{\rm gg}(\boldsymbol{k} + k_P \boldsymbol{n}) + \bar{n}^{-1} C_1(\boldsymbol{k}), \tag{A4}$$

where the sum is over three-dimensional integer lattice $\boldsymbol{n} = (n_1, n_2, n_3)$, $\hat{W}_{\rm g}$ is the Fourier transform of $W_{\rm g}$:

$$\hat{W}_{\rm g}(\boldsymbol{k}) = \prod_{i=1}^{3} \left[\frac{\sin(\pi k_i / k_P)}{\pi k_i / k_P} \right]^2, \tag{A5}$$

where $k_P \equiv 2\pi N_{\rm grid}/L$ is the period of Fourier modes, $\bar{n} \equiv N/L^3$ is the mean number density, and the smoothed shot noise term is

$$C_1(\boldsymbol{k}) \equiv \sum_{\boldsymbol{n}} \left| \hat{W}_{\rm g}(\boldsymbol{k} + k_P \boldsymbol{n}) \right|^2 \tag{A6}$$

$$= \prod_{i=1}^{3} \left[1 - \frac{2}{3} \sin^2(\pi k_i / k_P) \right]. \tag{A7}$$

Discrete sampling introduces a periodicity in Fourier space with a period of k_P, and all modes higher than the Nyquist frequency $k_{\rm Nq} \equiv \pi N_{\rm grid}/L = k_P/2$ are added to the modes in $|k_i| \le k_{\rm Nq}$. This is known as aliasing. Because the power spectrum beyond the Nyquist frequency is not known a priori, the power spectrum is extrapolated by a power law beyond $k_{\rm Nq}$:

$$P_{\rm gg}(\boldsymbol{k} + k_P \boldsymbol{n}) \approx P_{\rm gg}(k) (|k + k_P \boldsymbol{n}|/k)^{n_{\rm eff}}. \tag{A8}$$

This $n_{\rm eff}$ can be determined iteratively, but we obtained sufficient accuracy by setting $n_{\rm eff} = -1.6$. This extrapolation makes it possible to calculate the smoothing factor C_2:

$$\tilde{P}_{\rm gg}(\boldsymbol{k}) \approx C_{2{\rm gg}}(\boldsymbol{k}) P_{\rm gg}(\boldsymbol{k}) + \bar{n}^{-1} C_1(\boldsymbol{k}), \tag{A9}$$

where

$$C_{2{\rm gg}}(\boldsymbol{k}) \equiv \sum_{\boldsymbol{n}} |\hat{W}_{\rm g}(\boldsymbol{k} + k_P \boldsymbol{n})|^2 \, (|\boldsymbol{k} + k_P \boldsymbol{n}|/k_P)^{n_{\rm eff}}. \tag{A10}$$

The corrected power spectrum $P_{\rm gg}(\boldsymbol{k})$ is calculated from the grid power spectrum $\tilde{P}_{\rm gg}(\boldsymbol{k})$ by first subtracting the shot noise, $\bar{n}^{-1} C_1(\boldsymbol{k})$, and then divided by $C_{2{\rm gg}}(\boldsymbol{k})$. We spherically averaged the power spectrum after the correction.

In the left-hand panel of Fig. A1, we plot the spherically averaged subhalo power spectrum before corrections, $\tilde{P}_{\rm gg}$, for different grid resolutions $N_{\rm grid} = 64, 128, 256$, and 512. The power spectra are plotted up to the Nyquist frequencies $k_{\rm Nq} = 0.20\,(N_{\rm grid}/64)$ for $L = 1\,h^{-1}$ Gpc. The grid power spectrum is smoothed near $k_{\rm Nq}$. In the left-hand panel of Fig. A2, we plot the ratio of grid power spectra after shot noise subtraction to the true power spectra, which is the $C_{2{\rm gg}}$ function in equation (A9). We first subtract the shot noise $C_1(\boldsymbol{k})$ from $\tilde{P}_{\rm gg}(\boldsymbol{k})$, take its spherical average, and then divide that by the true spherically averaged power spectrum $P_{\rm gg}(k)$, which is the corrected power spectrum for $N_{\rm grid} = 512$ here. The black curve on top of those simulation data is the spherically averaged theoretical curve (equation A10); we calculated the equation on a three-dimensional grid with $N_{\rm grid} = 256$, with finite sums for $n_i = -2, -1, 0$, and 1, and then took the spherical average. Because the function is rapidly decreasing with k, most of the aliases are negligible. Only the $n_i = -1$ aliases have comparable magnitude. This curve matches perfectly with the data points computed from simulation subhaloes. Finally, in the left-hand panel of Fig. A3, we plot the power spectrum after the correction. The power spectra with different grid resolution are consistent within 1 per cent for all $k \le k_{\rm Nq}$.

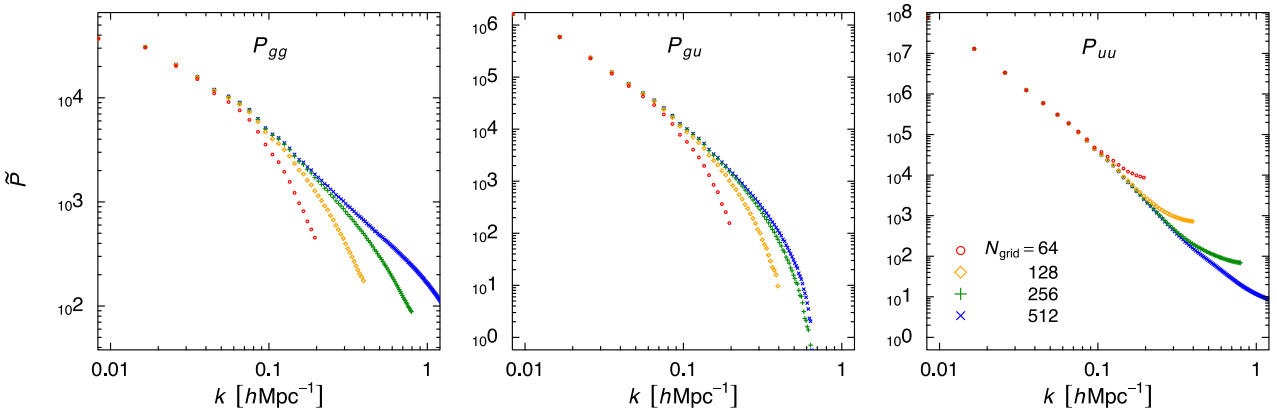

Figure A1. Power spectra before corrections. The auto- and cross-power spectra of subhalo density and line-of-sight peculiar velocity are calculated on grids with different resolutions $N_{\rm grid} = 64$, 128, 256, and 512. Left-hand panel is the subhalo–subhalo auto-power spectrum $\tilde{P}_{\rm gg}$, middle panel is the subhalo–velocity cross power $\tilde{P}_{\rm gu}$, and right-hand panel is the velocity–velocity autopower spectrum $\tilde{P}_{\rm uu}$. See the caption of Fig. 1 for the units of the power spectra.

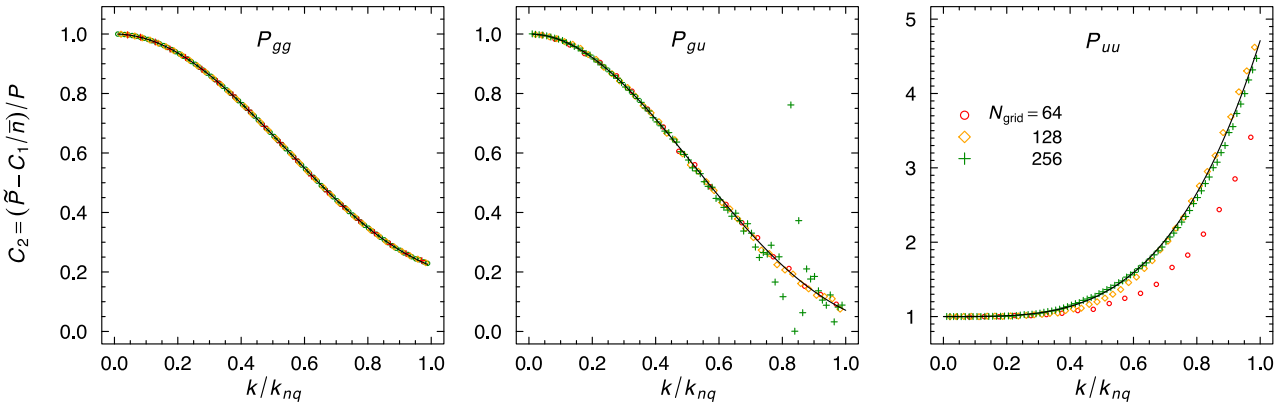

Figure A2. The ratio of power spectrum calculated on a grid to the true power spectrum (the shot noise C_1 is first subtracted from the subhalo autopower). The black curves are the C_2 functions we use to correct the gridding effect (equations A10, A13, and A16).

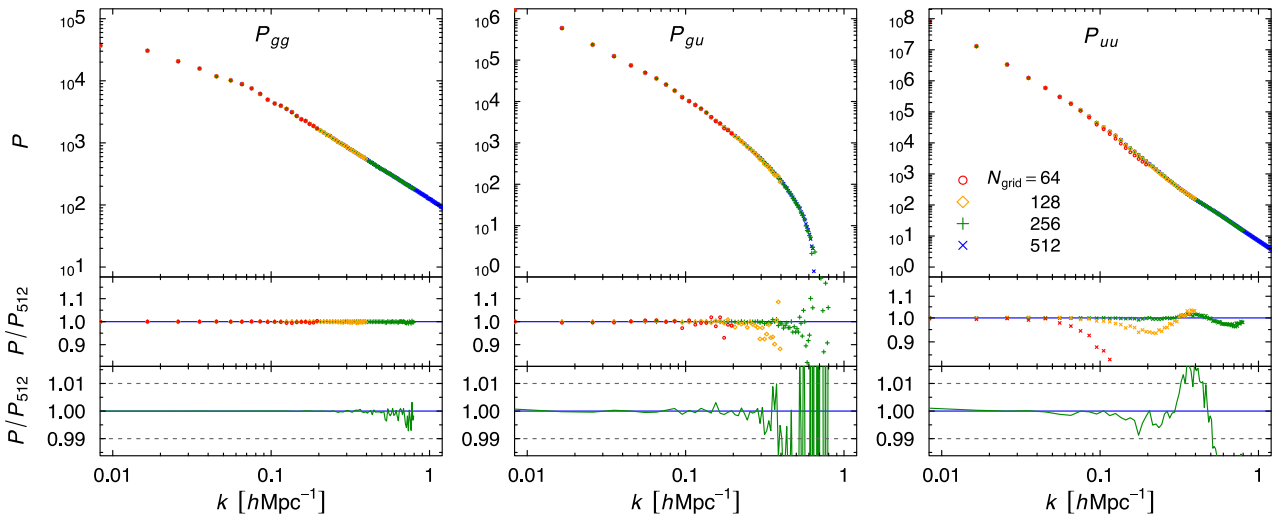

Figure A3. Power spectra after corrections (top panels), and relative difference compared with $N_{\rm grid} = 512$ power spectra at 10 per cent level (middle row) and 1 per cent level for $N_{\rm grid} = 256$ (bottom row). $N_{\rm grid} = 256$ converge within 1 per cent for $k \leq 0.3$.

A2 Field of nearest particle velocity

We use the nearest particle velocity to calculate the grid velocity field. For each grid point x_I, we find the particle nearest to the grid point, and set the grid velocity field $\tilde{u}(x_I)$ equal to the line-of-sight velocity of that particle. We apply this method for subhaloes whose number density is much lower than the number of grid points. Other methods could be suitable in the other limit of many particles per grid point; see also Section A3. We use the KD-TREE algorithm to find the nearest neighbour computationally efficient. The smooth field before gridding, for this method, is the piecewise constant velocity field which is equal to the particle velocity in each Voronoi cell (Bernardeau & van de Weygaert 1996):

$$u(\boldsymbol{x}) = \sum_a u_a \chi_a(\boldsymbol{x}), \tag{A11}$$

where $\chi_a(\boldsymbol{x}) = 1$ if the particle a is the nearest particle of point $\boldsymbol{x}$, and $\chi_a(\boldsymbol{x}) = 0$ otherwise. The window function of this nearest particle method is the Dirac delta function $W_{\rm u}(\boldsymbol{r}) = \delta_{\rm D}(\boldsymbol{r})$:

$$\tilde{u}(\boldsymbol{x}_I) = \int {\rm d}^3 y\, W_{\rm u}(\boldsymbol{x}_I - \boldsymbol{y}) u(\boldsymbol{y}). \tag{A12}$$

The Fourier transform of the window function is $\hat{W}_{\rm u}(\boldsymbol{k}) = 1$.

The advantages of our method are that (a) the velocity field on the grid converges to a meaningful velocity field $u(\boldsymbol{x})$ as $N_{\rm grid} \to \infty$, and (b) the assignment to grid points is done by a convolution (equation A12). Since nearest neighbour exists at any grid point, we do not have the problem of empty cells that the velocity field becomes undefined. Another common difficulty is that the smoothing kernel becomes spatially varying, not in the form of a convolution. Typically, the normalization factor depends on x_I, which makes the kernel in equation (A12) a function of $\boldsymbol{x}_I$ as well, $W_{\rm u}(\boldsymbol{x}_I - \boldsymbol{y}, \boldsymbol{x}_I)$. This would make the correction complicated, because the smoothed power $\tilde{P}(\boldsymbol{k})$ at wavenumber $\boldsymbol{k}$, would then depend on the power at all wavenumbers $P(\boldsymbol{k}')$, not only on the power at the same wavenumber $P(\boldsymbol{k})$.

In the middle and right-hand panels of Fig. A1, we plot the subhalo density–velocity cross-power $\tilde{P}_{\rm gu}$ and the velocity–velocity autopower $\tilde{P}_{\rm uu}$, respectively, calculated from CIC density and nearest particle velocity fields before any corrections. The cross-power has a smoothing, and the velocity autopower has an increase in power due to aliasing.

A2.1 Cross-power correction

In the middle panel of Fig. A2, we plot the angle-averaged cross-power calculated for $N_{\rm grid} = 64$, 128, and 256 divided by the angle-averaged $N_{\rm grid} = 512$ cross-power after the correction we will describe here. (The angle average is only performed in the upper-half of k space, i.e. $\int_0^1 {\rm d}\mu$.) Although we naively expect this ratio to be $\hat{W}_{\rm g}\hat{W}_{\rm u} = \hat{W}_{\rm g}$, because the density is smoothed by a factor of $\hat{W}_{\rm g}$ and the velocity field is smoothed by $\hat{W}_{\rm u}$, we find a smoothing closer to $\hat{W}_{\rm g}^{2.5}$. We fit the points by an empirical formula

$$C_{\rm 2gu}(k) \equiv \left[\frac{\sin(\pi k/k_P)}{\pi k/k_P}\right]^5 \left[1 - 0.27(k/k_{\rm Nq})^5\right], \tag{A13}$$

where $k_P = 2\pi N_{\rm grid}/L$ and $k_{\rm Nq} = k_P/2$ are the same as those in the previous section. This fitting formula is plotted by a black curve in the figure. We use this function to correct the cross-power:

$$P_{\rm gu}(\boldsymbol{k}) = \tilde{P}_{\rm gu}(\boldsymbol{k})/C_{\rm 2gu}(k). \tag{A14}$$

In the middle panel of Fig. A3, we plot the corrected cross-power. Although there are some scatter at high k, the $N_{\rm grid} = 256$ cross-power converge within 1 per cent for $k \le 0.3\,h\,{\rm Mpc}^{-1}$.

A2.2 Velocity autopower correction

In the right-hand panel of Fig. A2, we plot the ratio of the angle-averaged velocity autopower spectra calculated on a grid to that calculated with $N_{\rm grid} = 512$ with corrections. We do not subtract a component analogous to the shot noise C_1. This could be the reason that the $N_{\rm grid} = 64$ points do not match with other points. The C_2 function analogous to equation (A10) for velocity–velocity power spectrum with $W_{\rm u} = 1$ is

$$\begin{aligned} C_{\rm 2uu} &= \sum_{\boldsymbol{n}} (|\boldsymbol{k} + k_P\boldsymbol{n}|/k_P)^{n_{\rm eff}-2} \\ &= 1 + (k/k_{\rm Nq})^{n_{\rm eff}-2} \sum_{\boldsymbol{n}\neq\boldsymbol{0}} \left(\frac{\boldsymbol{k}}{2k} + \boldsymbol{n}\right)^{n_{\rm eff}-2}. \end{aligned} \tag{A15}$$

The exponent is $n_{\rm eff} - 2$, because velocity power spectra has an extra k^{-2} factor compared to matter power spectra in linear theory. This sum over integers converges very slowly, which makes it impractical to calculate $C_{\rm 2uu}(\boldsymbol{k})$ for all $\boldsymbol{k}$. We approximate the sum by a constant by fitting the points from the simulation for $N = 128$ and 256,

$$C_{\rm 2uu} \approx 1 + 3.7(k/k_{\rm Nq})^{n_{\rm neff}-2}. \tag{A16}$$

The constant pre-factor is consistent with equation (A15) for $\boldsymbol{k}$ near the Nyquist frequency. We correct the power spectrum with this formula

$$P_{\rm uu}(\boldsymbol{k}) = \tilde{P}_{\rm uu}(\boldsymbol{k})/C_{\rm 2uu}(k). \tag{A17}$$

The corrected power spectra is plotted in the right-hand panel of Fig. A3. The velocity autopower with $N_{\rm grid}$ also converges within 1 per cent for $k \le 0.3\,h\,{\rm Mpc}^{-1}$.

A3 Discussion on computing the velocity power spectrum

We presented our relatively simple method of using nearest particle velocity to calculate velocity power spectrum. Zheng et al. (2013) independently used a similar method to calculate the velocity power spectrum; see also their paper for various numerical convergence tests. A drawback of this method is that all high k aliases add to low k modes without smoothing, because the sampling function in Fourier space is a constant, not a rapidly declining function of k.

Calculating velocity power spectrum has technical difficulties that do not exist for density power spectrum. Calculating velocity by first assigning momentum on grids and then dividing them by density using a fixed kernel (e.g. CIC) has two problems. One is that the velocity becomes undefined if the density is zero. In the limit of infinite grids, velocity becomes undefined almost everywhere, which means there is no proper convergence as we increases the number of grids. Using adaptive kernel, in which the kernel length increases at low-density regions, can avoid the problem of undefined velocity (e.g. Mao et al. 2012), but the resulting velocity field is smoothed in a complicated way, for which it is difficult (not necessarily impossible, but at least computationally expensive) to deconvolve the kernel smoothing. The other problem is that, since the Fourier transformation is a volume integral, mixing mass-weighted average within grid cells make the convergence, as the number of grids increase, inefficient. Pueblas & Scoccimarro (2009) use volume-weighted average by calculating the volume from local Delaunay tessellation using

volumes that are entirely inside a grid cell. This improves the accuracy and convergence, but Delaunay tessellations spanning several cells are not treated accurately for simplicity, which is sufficient for a large number of particles, but becomes problematic for sparse samples, such as galaxies or haloes. Integration of velocity field to a grid cell is necessary (Bernardeau & van de Weygaert 1996).

The Delaunay Tessellation Field Estimator (DTFE) software[7] (Schaap & van de Weygaert 2000; Cautun & van de Weygaert 2011) is a publicly available code that calculates velocity field interpolated by the Delaunay tessellation, and integrating the field numerically on grids with the Monte Carlo approach. The DTFE software works well for velocity power spectrum, too (Jennings 2012). This Monte Carlo integration is a reasonable method to suppress the high k aliases, which can be added to improve our nearest particle method in the future if necessary.

APPENDIX B: THE FISHER MATRIX FOR MULTIPLE TRACERS

In this appendix, we first derive the Fisher matrix with the classical approximation in Section B1, and then drive other forms of the Fisher matrix in Sections B2 and B3.

B1 Derivation

We summarize the derivation of Fisher matrix using the 'classical approximation' (Hamilton 1997; Abramo 2012). This approximation simplifies the Fisher Matrix with spatially inhomogeneous noise to a form similar to that with constant noise.

Let $\phi_a(\boldsymbol{x})\,(a=1,\ldots,N)$ be N real Gaussian fields in configuration space which have zero mean, $\langle\phi_a(\boldsymbol{x})\rangle=0$. They can be a pair of galaxy density field and line-of-sight peculiar velocity, N galaxy density fields with different biases, or any multiple tracers of a random Gaussian field. We apply equation (11) to this continuously infinite number of Gaussian variables labelled by the position $\boldsymbol{x}$. The mean vector is zero, $\boldsymbol{\mu}=\boldsymbol{0}$, and the covariance matrix $\mathbf{C}$ is labelled by two positions $C_{mn}\rightarrow\Sigma_{ab}(\boldsymbol{x},\boldsymbol{y})\equiv\langle\phi_a(\boldsymbol{x})\phi_b(\boldsymbol{y})\rangle$, which are the auto- or cross-two-point correlation functions. In this continuous limit, sums over matrix indexes are replaced by integrals; equation (11) becomes

$$F_{ij}=\frac{1}{2}\int \mathrm{d}^3x\,\mathrm{d}^3x'\,\mathrm{d}^3y\,\mathrm{d}^3y' \times\mathrm{tr}\left[\Sigma^{-1}(\boldsymbol{x},\boldsymbol{x}')\frac{\partial\Sigma(\boldsymbol{x}',\boldsymbol{y})}{\partial\theta_i}\Sigma^{-1}(\boldsymbol{y},\boldsymbol{y}')\frac{\partial\Sigma(\boldsymbol{y}',\boldsymbol{x})}{\partial\theta_j}\right]. \quad \text{(B1)}$$

The inverse function is defined as

$$\int \mathrm{d}^3y\;\Sigma^{-1}(\boldsymbol{x},\boldsymbol{y})\Sigma(\boldsymbol{y},\boldsymbol{z})=I_N\delta_{\mathrm{D}}(\boldsymbol{x}-\boldsymbol{z}) \quad \text{(B2)}$$

and

$$\int \mathrm{d}^3y\;\Sigma(\boldsymbol{x},\boldsymbol{y})\Sigma^{-1}(\boldsymbol{y},\boldsymbol{z})=I_N\delta_{\mathrm{D}}(\boldsymbol{x}-\boldsymbol{z}), \quad \text{(B3)}$$

where I_N is the $N\times N$ unit matrix.

The covariance function $\Sigma(\boldsymbol{x},\boldsymbol{y})$ contains translationally invariant correlation functions ξ_{ab}, and spatially uncorrelated noise terms N_{ab}:

$$\Sigma_{ab}(\boldsymbol{x},\boldsymbol{y})=\xi_{ab}(\boldsymbol{x}-\boldsymbol{y})+N_{ab}(\boldsymbol{x})\delta_{\mathrm{D}}(\boldsymbol{x}-\boldsymbol{y}), \quad \text{(B4)}$$

where δ_{D} is the Dirac delta function.

[7] http://www.astro.rug.nl/\~voronoi/DTFE/dtfe.html

For a pair of galaxy density contrast field, $\phi_1=\delta_{\mathrm{g}}$, and line-of-sight velocity $\phi_2=u$, the matrix of correlation functions is

$$\Sigma(\boldsymbol{x},\boldsymbol{y})=\begin{pmatrix}\xi_{\mathrm{gg}}(\boldsymbol{x}-\boldsymbol{y})+N_{\mathrm{g}} & \xi_{\mathrm{gu}}(\boldsymbol{x}-\boldsymbol{y})\\ \xi_{\mathrm{ug}}(\boldsymbol{x}-\boldsymbol{y}) & \xi_{\mathrm{uu}}(\boldsymbol{x}-\boldsymbol{y})+N_{\mathrm{u}}\end{pmatrix}. \quad \text{(B5)}$$

The noise term for the density contrast, N_{g}, is the shot noise:

$$N_{\mathrm{g}}(\boldsymbol{x},\boldsymbol{y})=n_{\mathrm{g}}^{-1}(\boldsymbol{x})\delta_{\mathrm{D}}(\boldsymbol{x}-\boldsymbol{y}), \quad \text{(B6)}$$

where $n_{\mathrm{g}}(\boldsymbol{x})$ is the smooth ensemble mean number density of galaxies. Similarly, N_{g} is the noise in peculiar velocity measurement:

$$N_{\mathrm{u}}(\boldsymbol{x},\boldsymbol{y})=n_{\mathrm{u}}^{-1}(\boldsymbol{x})\sigma^2_{\mathrm{u\text{-}noise}}(\boldsymbol{x})\delta_{\mathrm{D}}(\boldsymbol{x}-\boldsymbol{y}), \quad \text{(B7)}$$

where $n_{\mathrm{u}}(\boldsymbol{x})$ is the mean number density of galaxies with peculiar velocity measurements, and σ_{vobs} is the observational error in peculiar velocity per galaxy.

Using the fact that a two-point correlation function ξ_{ab} is the Fourier transform of the corresponding power spectrum P_{ab}, we can write $\Sigma(\boldsymbol{x},\boldsymbol{y})$ with power spectra:

$$\Sigma(\boldsymbol{x},\boldsymbol{y})=\int\frac{\mathrm{d}^3k}{(2\pi)^3}\tilde{\Sigma}(\boldsymbol{k},\boldsymbol{x})\mathrm{e}^{\mathrm{i}\boldsymbol{k}\cdot(\boldsymbol{x}-\boldsymbol{y})}, \quad \text{(B8)}$$

where

$$\tilde{\Sigma}(\boldsymbol{k},\boldsymbol{x})_{ab}\equiv P_{ab}(\boldsymbol{k})+N_{ab}(\boldsymbol{x}). \quad \text{(B9)}$$

Equation (B5), for a case of density and velocity, transforms to

$$\tilde{\Sigma}(\boldsymbol{k},\boldsymbol{x})=\begin{pmatrix}P_{\mathrm{gg}}(\boldsymbol{k})+n_{\mathrm{g}}^{-1}(\boldsymbol{x}) & P_{\mathrm{gu}}(\boldsymbol{k})\\ P_{\mathrm{ug}}(\boldsymbol{k}) & P_{\mathrm{uu}}(\boldsymbol{k})+n_{\mathrm{u}}^{-1}\sigma^2_{\mathrm{u\text{-}noise}}\end{pmatrix}. \quad \text{(B10)}$$

[$P_{\mathrm{ug}}(\boldsymbol{k})=\langle u(\boldsymbol{k})\delta_{\mathrm{g}}(\boldsymbol{k})^*\rangle$ is the complex conjugate of $P_{\mathrm{gu}}(\boldsymbol{k})$.] For N biased galaxy tracers with biases b_i and mean number density $n_i(\boldsymbol{x})$, $\tilde{\Sigma}$ matrix is, e.g.

$$\tilde{\Sigma}_{ab}(\boldsymbol{k},\boldsymbol{x})=b_ib_j(1+\beta_i\mu^2)(1+\beta_j\mu^2)P_{\mathrm{m}}(\boldsymbol{k})+n_i^{-1}(\boldsymbol{x})\delta_{ab}, \quad \text{(B11)}$$

where $\beta_i\equiv f/b_i$, for the simplest case of the linear theory.

The delta functions in the noise terms enable us to replace $\boldsymbol{x}$ by $\boldsymbol{y}$, if necessary,

$$\Sigma(\boldsymbol{x},\boldsymbol{y})=\int\frac{\mathrm{d}^3k}{(2\pi)^3}\tilde{\Sigma}(\boldsymbol{k},\boldsymbol{y})\mathrm{e}^{\mathrm{i}\boldsymbol{k}\cdot(\boldsymbol{x}-\boldsymbol{y})}. \quad \text{(B12)}$$

A symmetry in correlation function, $\Sigma_{ab}(\boldsymbol{x},\boldsymbol{y})=\Sigma_{ba}(\boldsymbol{y},\boldsymbol{x})$, by definition, propagates to a property that $\tilde{\Sigma}$ is a Hermitian matrix: $\tilde{\Sigma}_{ab}(\boldsymbol{k},\boldsymbol{x})=\tilde{\Sigma}_{ba}(\boldsymbol{k},\boldsymbol{x})^*$. The matrix $\tilde{\Sigma}$ is a real symmetric matrix for density contrasts of multitracers, but for density and peculiar velocity, the off-diagonal term P_{gu} is pure imaginary as a result of parity invariance, as we discussed in Section 2.

The 'classical approximation' (Hamilton 1997) allows us to approximate the inverse function by the inverse matrix in Fourier space:

$$\Sigma^{-1}(\boldsymbol{x},\boldsymbol{y})\approx\int\frac{\mathrm{d}^3k}{(2\pi)^3}\tilde{\Sigma}(\boldsymbol{k},\boldsymbol{x})^{-1}\mathrm{e}^{\mathrm{i}\boldsymbol{k}\cdot(\boldsymbol{x}-\boldsymbol{y})}, \quad \text{(B13)}$$

where $\tilde{\Sigma}(\boldsymbol{k},\boldsymbol{x})^{-1}$ is the inverse matrix of $\tilde{\Sigma}(\boldsymbol{k},\boldsymbol{x})$ for fixed $\boldsymbol{x}$ and $\boldsymbol{k}$. To check that is approximately an inverse function, equations (B12) and (B13) substituted to the left-hand side of equation (B2) give

$$\int\frac{\mathrm{d}^3k}{(2\pi)^3}\tilde{\Sigma}(\boldsymbol{k},\boldsymbol{x})^{-1}\tilde{\Sigma}(\boldsymbol{k},\boldsymbol{z})\mathrm{e}^{\mathrm{i}\boldsymbol{k}\cdot(\boldsymbol{x}-\boldsymbol{z})}. \quad \text{(B14)}$$

If (a) $\boldsymbol{x}\approx\boldsymbol{z}$, such that the noise terms $N(\boldsymbol{x})$ and $N(\boldsymbol{z})$ are approximately equal to each other, then $\tilde{\Sigma}(\boldsymbol{k},\boldsymbol{x})^{-1}\tilde{\Sigma}(\boldsymbol{k},\boldsymbol{z})\approx I_N$ makes equation (B14) equal the right-hand side of equation (B2). If (b) $\boldsymbol{x}$ and $\boldsymbol{z}$ are far enough from each other, then $\mathrm{e}^{\mathrm{i}\boldsymbol{k}\cdot(\boldsymbol{x}-\boldsymbol{z})}$ is a rapidly oscillating function of $\boldsymbol{k}$, which makes the integral in equation (B14)

approximately zero – again the equation (B2) is satisfied. Because the integrand depends on $\boldsymbol{k}$ through $P_{ab}(\boldsymbol{k})$, the approximation that the rapid oscillation makes the integral vanishing is reasonable if $\int \frac{\mathrm{d}^3k}{(2\pi)^3} P_{ab}(\boldsymbol{k}) \mathrm{e}^{\mathrm{i}\boldsymbol{k}\cdot(\boldsymbol{x}-\boldsymbol{z})} = \xi_{ab}(\boldsymbol{x}-\boldsymbol{z}) \approx 0$. In summary, the approximation used here, called the classical approximation, is valid if either (a) or (b) is satisfied for all values of $\boldsymbol{x}-\boldsymbol{z}$. This means that the noise terms are approximately constant within the coherence length, where the two-point correlation functions are not negligible. Equation (B3) can be shown in the same way. Although this approximation is usually satisfied for redshift surveys, it requires more caution for peculiar velocity surveys due to larger coherence length, and distant-dependent observational noise term σ_{vobs}.

Substituting the inverse function (equation B13) into the Fisher matrix equation (B1) gives

$$F_{ij} = \frac{1}{2}\int \mathrm{d}^3x\,\mathrm{d}^3y \frac{\mathrm{d}^3k}{(2\pi)^3}\frac{\mathrm{d}^3q}{(2\pi)^3}\mathrm{e}^{\mathrm{i}(\boldsymbol{k}-\boldsymbol{q})\cdot(\boldsymbol{x}-\boldsymbol{y})} \times \mathrm{tr}\left[\tilde{\Sigma}^{-1}(\boldsymbol{k},\boldsymbol{x})\frac{\partial\tilde{\Sigma}}{\partial\theta_i}(\boldsymbol{k})\tilde{\Sigma}^{-1}(\boldsymbol{q},\boldsymbol{y})\frac{\partial\tilde{\Sigma}}{\partial\theta_j}(\boldsymbol{q})\right], \quad \text{(B15)}$$

where we use the assumption that the noise terms are determined from observations, not directly related to cosmological parameters, i.e.

$$\frac{\partial\tilde{\Sigma}(\boldsymbol{k},\boldsymbol{x})}{\partial\theta_i} = \frac{\partial P(\boldsymbol{k})}{\partial\theta_i} \quad \text{(B16)}$$

is a function of $\boldsymbol{k}$ only. Using the same argument of the classical approximation, the k and q integrals are negligible for large $\boldsymbol{x}-\boldsymbol{y}$ due to rapid oscillation of the exponential term. Therefore, the dominant contribution comes from $\boldsymbol{x}\approx\boldsymbol{y}$, which allows us to replace, $\tilde{\Sigma}(\boldsymbol{q},\boldsymbol{y})^{-1} \approx \tilde{\Sigma}(\boldsymbol{q},\boldsymbol{x})^{-1}$. We can then rearrange the integral $\int \mathrm{d}^3x\,\mathrm{d}^3y = \int \mathrm{d}^3x\,\mathrm{d}^3(x-y)$ and perform the $\mathrm{d}^3(x-y)$ integral. This gives our final result for the Fisher Matrix:

$$F_{ij} = \frac{1}{2}\int \frac{\mathrm{d}^3x\,\mathrm{d}^3k}{(2\pi)^3}\,\mathrm{tr}\left[\tilde{\Sigma}(\boldsymbol{k},\boldsymbol{x})^{-1}\frac{\partial\tilde{\Sigma}}{\partial\theta_i}\tilde{\Sigma}(\boldsymbol{k},\boldsymbol{x})^{-1}\frac{\partial\tilde{\Sigma}}{\partial\theta_j}\right], \quad \text{(B17)}$$

where all $\tilde{\Sigma}$ are evaluated at $\boldsymbol{k}$ and $\boldsymbol{x}$. For a single field, this reduces to the Fisher matrix by Tegmark (1997) with Feldman, Kaiser & Peacock (1994) minimum variance. The virtue of this derivation, starting from the Gaussian fields in configuration space, is that this minimum variance appears automatically, and the generalization to multiple fields is straightforward.

B2 Isomorphic transformation

The Fisher matrix is invariant under any invertible linear transformation (isomorphism) $\phi' = A\phi$ between statistically translational invariant fields if that transformation does not include any uncertain parameters θ_i. For example, BT04 use line-of-sight velocity gradient $\phi' \equiv (\delta_{\mathrm{g}}, \partial u/\partial r)$, instead of velocity, $\phi = (\delta_{\mathrm{g}}, u)$; we show that the Fisher matrix for ϕ' is exactly equal to that for ϕ. This is one of the two steps that their Fisher matrix is exactly equal to what we use in this paper.

Since our formalism is based on an assumption that the field is translationally invariant (e.g. equation B4), we require that the linear transformation conserves translational invariance. Such transformation is a convolution in configuration space, which is a multiplication in Fourier space:

$$\phi'(\boldsymbol{k}) = \mathbf{A}(\boldsymbol{k})\phi(\boldsymbol{k}). \quad \text{(B18)}$$

We require that $\mathbf{A}$ is a $N\times N$ matrix that has an inverse $\mathbf{A}^{-1}$, and it does not depend on parameters θ_i. The matrix of power spectra $\tilde{\Sigma}'$ (equation B8) for ϕ' is related to the original matrix by

$$\tilde{\Sigma}'(\boldsymbol{k},\boldsymbol{x}) = \mathbf{A}(\boldsymbol{k})\tilde{\Sigma}(\boldsymbol{k},\boldsymbol{x})\mathbf{A}^{\dagger}(\boldsymbol{k}), \quad \text{(B19)}$$

where $\mathbf{A}^{\dagger}$ is the Hermitian conjugate of $\mathbf{A}$. Such transformation does not change the trace:

$$\mathrm{tr}\left[\Sigma'^{-1}\frac{\partial\Sigma'}{\partial\theta_i}\Sigma'^{-1}\frac{\partial\Sigma'}{\partial\theta_j}\right] = \mathrm{tr}\left[\Sigma^{-1}\frac{\partial\Sigma}{\partial\theta_i}\Sigma^{-1}\frac{\partial\Sigma}{\partial\theta_j}\right] \quad \text{(B20)}$$

for each value of $\boldsymbol{k}$ and $\boldsymbol{x}$ because all $\mathbf{A}$ matrices cancels their inverse matrices in the trace. This proves what we stated at the beginning of this section.

B2.1 Lemma

The Fisher matrix (equation B17) is invariant under any isomorphism, $\phi' = \mathbf{A}\phi$ (equation B18), if it does not contain any of the parameters θ_i. The Fisher matrix formula with ϕ' is exactly equal to that with ϕ.

B2.2 Examples of isomorphism

The aforementioned example of using velocity gradient (BT04) is a transformation:

$$\phi'(\boldsymbol{k}) = \mathbf{A}\phi = \begin{pmatrix} 1 & 0 \\ 0 & \mathrm{i}k\mu \end{pmatrix}\begin{pmatrix} \delta_{\mathrm{g}}(\boldsymbol{k}) \\ u(\boldsymbol{k}) \end{pmatrix}, \quad \text{(B21)}$$

with flat-sky approximation, where μ is the cosine of the angle between $\boldsymbol{k}$ and the fixed line-of-sight direction. (This matrix is invertible for $\boldsymbol{k}\neq 0$, and $\boldsymbol{k}=\boldsymbol{0}$ mode of velocity is zero, not carrying any cosmological information.) The covariance matrix transforms as

$$\tilde{\Sigma}' = \mathbf{A}\tilde{\Sigma}\mathbf{A}^{\dagger} = \begin{pmatrix} \tilde{\Sigma}_{11} & -\mathrm{i}k\mu\tilde{\Sigma}_{11} \\ \mathrm{i}k\mu\tilde{\Sigma}_{22} & k^2\mu^2\tilde{\Sigma}_{22} \end{pmatrix}. \quad \text{(B22)}$$

Although the covariance matrices $\tilde{\Sigma}$ and $\tilde{\Sigma}'$ look different, the Fisher matrices calculated from those are exactly equal to each other.

We can also remove the imaginary number i from cross-power spectra without changing the Fisher matrix. Applying a matrix,

$$\tilde{\phi}(\boldsymbol{k}) \equiv \begin{pmatrix} \delta_{\mathrm{g}}(\boldsymbol{k}) \\ \tilde{u}(\boldsymbol{k}) \end{pmatrix} \equiv \mathbf{A}\phi = \begin{pmatrix} 1 & 0 \\ 0 & \mathrm{i} \end{pmatrix}\begin{pmatrix} \delta_{\mathrm{g}}(\boldsymbol{k}) \\ u(\boldsymbol{k}) \end{pmatrix}, \quad \text{(B23)}$$

transforms the cross power to a real function. Our lemma guarantees that the Fisher matrix remains exactly the same.

B3 Fisher matrix with power spectra covariance matrix

We derive an equivalent form of the Fisher matrix that is written with a covariance matrix of power spectra. Such Fisher matrices appear in BT04 and White, Song & Percival (2009). White et al. (2009) checked that two forms of Fisher matrix give the same numerical result. Here we show that the two formulae are algebraically equivalent.

Let us introduce N complex Gaussian variables with zero mean, $\delta_a(\boldsymbol{k},\boldsymbol{x})$, for each pair of $\boldsymbol{k}$ and $\boldsymbol{x}$ that is uniquely characterized by the covariance matrix:

$$\mathrm{Cov}(\delta_a,\delta_b) \equiv \langle\delta_a\delta_b^*\rangle = \tilde{\Sigma}_{ab}(\boldsymbol{k},\boldsymbol{x}), \quad \text{(B24)}$$

$$\mathrm{Cov}(\delta_a,\delta_b^*) = \langle\delta_a\delta_b\rangle = 0, \quad \text{(B25)}$$

where $\tilde{\Sigma}(\boldsymbol{k}, \boldsymbol{x})$ is the Hermitian matrix defined in equation (B8). These δ variables can be regarded as $\phi_a(\boldsymbol{k})$ in Fourier space when the noise terms are spatially homogeneous. When the noise terms were position dependent, it much clearer to define δ_a as a pure mathematical tool that assists the derivation, than to make this exact derivation inexact by going though the classical approximation again. We have shown that cross-power spectra are either real or pure imaginary, and when they are pure imaginary they can be converted to real cross-power without changing the Fisher matrix. We can therefore assume, without loss of generality, that $\tilde{\Sigma}$ is a real symmetric matrix.

The trace term in the Fisher Matrix (equation B17), with equation (B16), can be rewritten as

$$\mathrm{tr}\left[\tilde{\Sigma}^{-1}\frac{\partial P}{\partial\theta_i}\tilde{\Sigma}^{-1}\frac{\partial P}{\partial\theta_j}\right] = \frac{\partial P^*_{ab}}{\partial\theta_i}\Omega_{abcd}\frac{\partial P_{cd}}{\partial\theta_j}, \tag{B26}$$

where

$$\Omega_{abcd} \equiv \tilde{\Sigma}^{-1}_{ac}\tilde{\Sigma}^{-1}_{db}. \tag{B27}$$

All repeated indices are summed over $1, \ldots, N$. Consider $\boldsymbol{P}$ as a N^2 dimensional vector whose elements are P_{ab}, and Ω_{abcd} as $N^2 \times N^2$ matrix; equation (B26) is $(\partial \boldsymbol{P}^\dagger/\partial\theta_i)\Omega(\partial \boldsymbol{P}/\partial\theta_j)$ with this notation. The inverse matrix of Ω is the Ξ matrix, defined as

$$\Xi_{abcd} \equiv \tilde{\Sigma}_{ac}\tilde{\Sigma}_{db}. \tag{B28}$$

This can be checked by a calculation $\Omega_{abcd}\Xi_{cdef} = \delta_{ae}\delta_{bf}$ (δ_{ab} is the Kronecker's delta), which means $\Omega\Xi = I_{N^2}$ in matrix notation. This Ξ matrix turns out to be a covariance matrix of $\hat{P}_{ab}$ random variables,

$$\hat{P}_{ab} \equiv \delta_a\delta^*_b, \tag{B29}$$

because

$$\begin{aligned}\mathrm{Cov}(\hat{P}_{ab}, \hat{P}_{cd}) &\equiv \langle\delta_a\delta^*_b(\delta_c\delta^*_d)^*\rangle - \langle\delta_a\delta^*_b\rangle\langle(\delta_c\delta^*_d)^*\rangle \\ &= \langle\delta_a\delta^*_c\rangle\langle\delta_d\delta^*_b\rangle + \langle\delta_a\delta_d\rangle\langle\delta^*_b\delta^*_d\rangle \\ &= \tilde{\Sigma}_{ac}\tilde{\Sigma}_{db} = \Xi_{abcd},\end{aligned} \tag{B30}$$

or $\mathrm{Cov}(\hat{\boldsymbol{P}}, \hat{\boldsymbol{P}}) = \Xi$ in matrix notation, where the Isserlis' theorem or the Wick's theorem for Gaussian variables is used. We therefore got the other expression equivalent to the equation (B17):

$$F_{ij} = \frac{1}{2}\int\frac{\mathrm{d}^3x\,\mathrm{d}^3k}{(2\pi)^3}\frac{\partial \boldsymbol{P}^\dagger}{\partial\theta_i}\mathrm{Cov}(\hat{\boldsymbol{P}}, \hat{\boldsymbol{P}})^{-1}\frac{\partial \boldsymbol{P}}{\partial\theta_j}. \tag{B31}$$

This is a multiplication of N^2-dimensional vectors of power spectra with the covariance matrix of their N^4 pairs.

We now reduce the N^2-dimensional vector to $N(N+1)/2$-dimensional vector using the assumption that $\tilde{\Sigma}_{ab}$ is a real symmetric matrix. Let $\mathbf{R}$ be a $N^2 \times N^2$ invertible matrix with 1 and $\pm1/2$, such that $\boldsymbol{P}' \equiv (\boldsymbol{P}_{\rm sym}, \boldsymbol{P}_{\rm asym}) = \mathbf{R}\boldsymbol{P}$ become the symmetric and asymmetric combinations of P:

$$P^{\rm sym}_{ab} = \frac{1}{2}(P_{ab} + P_{ba}) \quad \text{for } a \le b, \tag{B32}$$

$$P^{\rm asym}_{ab} = \frac{1}{2}(P_{ab} - P_{ba}) \quad \text{for } a > b. \tag{B33}$$

The $N(N+1)/2$-dimensional vector $\boldsymbol{P}_{\rm sym}$ contains N autopower spectra and $N(N-1)/2$ symmetrized cross-power spectra. $\boldsymbol{P}_{\rm asym}$ contains $N(N-1)/2$ antisymmetrized cross-power spectra, which vanish by our assumption of symmetric power spectra: $\boldsymbol{P}_{\rm asym} = 0$.

The vector of rearranged power spectra estimator, $(\hat{\boldsymbol{P}}_{\rm sym}, \hat{\boldsymbol{P}}_{\rm asym}) \equiv \hat{\boldsymbol{P}}' \equiv R\hat{\boldsymbol{P}}$, has a covariance matrix

$$\Xi' \equiv \mathrm{Cov}(\hat{\boldsymbol{P}}', \hat{\boldsymbol{P}}') = R\Xi R^\dagger. \tag{B34}$$

The integrand of the Fisher matrix equation (B31) maintains the same form under this rearrangement:

$$\frac{\partial \boldsymbol{P}'^\dagger}{\partial\theta_i}\Xi'^{-1}\frac{\partial \boldsymbol{P}'}{\partial\theta_j} = \frac{\partial \boldsymbol{P}^\dagger}{\partial\theta_i}\Xi^{-1}\frac{\partial \boldsymbol{P}}{\partial\theta_j}. \tag{B35}$$

Finally, this Ξ' matrix is block diagonal

$$\Xi' = \begin{pmatrix}\Xi'_{\rm sym} & 0\\ 0 & \Xi'_{\rm asym}\end{pmatrix}, \tag{B36}$$

where $\Xi'_{\rm sym} \equiv \mathrm{Cov}(\hat{\boldsymbol{P}}_{\rm sym}, \hat{\boldsymbol{P}}_{\rm sym})$ and $\Xi'_{\rm asym} \equiv \mathrm{Cov}(\hat{\boldsymbol{P}}_{\rm asym}, \hat{\boldsymbol{P}}_{\rm asym})$, respectively, because the off-diagonal block vanishes,

$$\mathrm{Cov}(\delta_a\delta^*_b + \delta_b\delta^*_a, \delta_c\delta^*_d + \delta_d\delta^*_c) = 0, \tag{B37}$$

by straightforward calculation using the Wick theorem and the assumption $\tilde{\Sigma}_{ab} = \tilde{\Sigma}_{ba}$. Therefore the inverse matrix of Ξ is also block diagonal $\Xi^{-1} = \mathrm{diag}(\Xi^{-1}_{\rm sym}, \Xi^{-1}_{\rm asym})$. Note that the random vector $\hat{\boldsymbol{P}}_{\rm asym}$ is not zero – only its mean is zero. The matrix $\Xi_{\rm asym}$ is not a zero matrix either. Finally, we can reduce equation (B35) to $N(N+1)/2$-dimensional subspace using the inverse matrix and $\boldsymbol{P}_{\rm asym} = 0$:

$$\frac{\partial \boldsymbol{P}'^\dagger}{\partial\theta_i}\Xi'^{-1}\frac{\partial \boldsymbol{P}'}{\partial\theta_j} = \frac{\partial \boldsymbol{P}^\dagger_{\rm sym}}{\partial\theta_i}\Xi^{-1}_{\rm sym}\frac{\partial \boldsymbol{P}_{\rm sym}}{\partial\theta_j}. \tag{B38}$$

We complete the proof of the theorem summarized as follows.

B3.1 Theorem

The Fisher matrix of N Gaussian random fields with classical approximation (equation B17) is equal to the following Fisher matrix, when the matrix $\tilde{\Sigma}$ is a real symmetric matrix (which is always possible by transforming the field variables if necessary):

$$F_{ij} = \frac{1}{2}\int\frac{\mathrm{d}^3x\,\mathrm{d}^3k}{(2\pi)^3}\frac{\partial \boldsymbol{P}}{\partial\theta_i}\mathrm{Cov}(\hat{\boldsymbol{P}}_{\rm sym}, \hat{\boldsymbol{P}}_{\rm sym})^{-1}\frac{\partial \boldsymbol{P}}{\partial\theta_j}, \tag{B39}$$

where $\boldsymbol{P}(\boldsymbol{k})$ is a $N(N+1)/2$-dimensional vector of auto- and cross-power spectra $P_{ab}(a \le b)$, and the covariance matrix can be calculated from a vector of random variables $\hat{\boldsymbol{P}}_{\rm sym}$,[8]

$$\hat{P}^{\rm sym}_{ab} = \frac{1}{2}(\delta_a\delta^*_b + \delta_b\delta^*_a) - N_{ab}, \tag{B40}$$

defined by N random Gaussian variables $\delta_a(\boldsymbol{k}, \boldsymbol{x})$ (equations B24–B25). The covariance matrix can be written in terms of $\langle\delta_a\delta^*_b\rangle = \tilde{\Sigma}_{ab}(\boldsymbol{k}, \boldsymbol{x}) = P_{ab}(\boldsymbol{k}) + N_{ab}(\boldsymbol{x})$, using the Wick theorem. Note that $\delta_a\delta^*_b$ and $\delta_b\delta^*_a$ have the same expectation value, $\langle\delta_a\delta^*_b\rangle = \langle\delta_b\delta^*_a\rangle = P_{ab}$, but are different random variables; symmetrization in equation (B40) is necessary.

B3.2 An example of power spectra covariance matrix

This is an example of the covariance matrix $\mathrm{Cov}(\hat{\boldsymbol{P}}, \hat{\boldsymbol{P}})$ for two fields:

$$\mathrm{Cov}(\hat{P}_{11}, \hat{P}_{11}) = \tilde{\Sigma}^2_{11}, \tag{B41}$$

[8] Subtraction of the noise term is not necessary but the power spectra estimator is often written this way; covariance matrix does not change by subtracting constant values.

$$\mathrm{Cov}(\hat{P}_{11}, \hat{P}_{12}) = \tilde{\Sigma}_{11}\tilde{\Sigma}_{12}, \tag{B42}$$

$$\mathrm{Cov}(\hat{P}_{11}, \hat{P}_{22}) = \tilde{\Sigma}_{12}^2, \tag{B43}$$

$$\mathrm{Cov}(\hat{P}_{12}, \hat{P}_{12}) = \left(\tilde{\Sigma}_{11}\tilde{\Sigma}_{22} + \tilde{\Sigma}_{12}^2\right)/2, \tag{B44}$$

$$\mathrm{Cov}(\hat{P}_{12}, \hat{P}_{22}) = \tilde{\Sigma}_{12}\tilde{\Sigma}_{22}, \tag{B45}$$

$$\mathrm{Cov}(\hat{P}_{22}, \hat{P}_{22}) = \tilde{\Sigma}_{22}^2. \tag{B46}$$

Similar examples are in BT04 and White et al. (2009). They have factor of 2 larger covariance matrix instead of a factor of $1/2$ in equation (B39), which results in the same Fisher matrix. The location of the factor of 2 only reflects the definition of 'one Fourier mode', which does not change the overall equation.

For galaxy density contrast $\delta_{\rm g}^{\rm s}$ and transformed line-of-sight velocity $\tilde{u}^{\rm s} = {\rm i}u^{\rm s}$ (equation B23), which give real-number power spectra, the $\tilde{\Sigma}$ matrix elements are

$$\tilde{\Sigma}_{11} = P_{\rm gg}^{\rm s}(\boldsymbol{k}) + n_{\rm g}^{-1}(\boldsymbol{x}), \tag{B47}$$

$$\tilde{\Sigma}_{12} = P_{\rm gu}^{\rm s}(\boldsymbol{k}), \tag{B48}$$

$$\tilde{\Sigma}_{22} = P_{\rm uu}^{\rm s}(\boldsymbol{k}) + n_{\rm u}^{-1}(\boldsymbol{x})\sigma_{\rm u\text{-}noise}(\boldsymbol{x}). \tag{B49}$$

The same equation holds for galaxy density $\delta_{\rm g}$ and velocity gradient u', using the conversion of power spectra in Section B2.2. As a corollary of Appendices B2 and B3, we show that our Fisher matrix formula equation (15) is exactly the same Fisher matrix formula used in BT04, which is written with a covariance matrix of density and velocity gradient power spectra.

This paper has been typeset from a TEX/LATEX file prepared by the author.